CARBON QUANTUM DOTS SYNTHESIS SIMULATION

MECHANISM INVESTIGATION OF SYNTHESIZING CARBON QUANTUM DOTS FROM COAL BY NUMERICAL SIMULATION

By QI (KELLY) WANG, B.A.

A Thesis Submitted to the School of Graduate Studies in Partial Fulfillment of the Requirements for

the Degree Master of Applied Science

McMaster University MASTER OF APPLIED SCIENCE (2022) Hamilton, Ontario

Department of Materials Science and Engineering, Engineering Graduate Program

TITLE: Mechanism investigation of synthesizing carbon quantum dots from coal by numerical simulation

AUTHOR: Qi (Kelly) Wang, B.A. (South China University of Technology)

SUPERVISOR: Dr. Gu Xu

NUMBER OF PAGES: 107

Abstract

As fluorescent nanomaterial with excellent properties, carbon quantum dots have attracted significant attention. In particular, the synthesizing of carbon quantum dots has become the focus of various studies. Among them, carbon quantum dots synthesized from coal by strong acid oxidation have been widely studied for mass production. However, the broad size distribution of the products restricts their development, thereby prompting an issue that needs to be urgently resolved. Therefore, in this study, to achieve the control of size distribution, we simulated the diffusion process, in which sulfuric acid is inserted into the graphene layers of coal and destroys the van der Waals bonds. The result showed that when graphene layers are longer than 5 nm, the van der Waals bonds between them could not be broken within 10000 iterations. For bituminous carbon quantum dots, since its crystal structure size is small, the van der Waals bonds can be effectively broken, and narrow size distribution can be obtained at the 1500th iteration, which corresponds to the actual time of 34.2 h; for coke carbon quantum dots, since the crystal structure average size is larger than 5 nm, diffusion process cannot effectively break van der Waals bonds. The simulated result unravels the mechanism, guiding the experimental method to obtain a narrow size distribution and avoiding blind trials.

ACKNOWLEDGMENTS

First, I would like to sincerely gratitude to my supervisor Dr. Gu Xu for his tireless teaching and careful guidance for my research, who gave me the opportunity to complete my studies, from topic selection to conception to defense, his suggestions have always played a key role in my research. Besides, Dr. Gu Xu not only gave me careful guidance in my studies, but also gave me meticulous care in my life.

Secondly，I would like to appreciate my committee members who took the time out of their busy schedules to review and comment on my research and participate in my thesis defense. And I want to give my appreciation to all the professors who have instructed me, the technicians, and staff who have helped me with my research.

Thirdly, I would also like to thank my colleagues in Xu's Research Group, Dr. Ryan T. Wang, Jason Y. Chen, Dr. Alex F. Xu, and Sonia L. Tai, for their support and assistance with my research. I would also like to thank my family and friends for their encouragement and company.

Table of contents

List of Figures

composites. HR-TEM analysis results of (e) CdS, (f) $CdIn_2S_4$, and (g) Carbon quantum dots. Broad spectrum response flower spherical-like composites CQDs@CdIn2S4/CdS modified by CQDs with up-conversion property for photocatalytic degradation and water splitting. Reprinted from (Huang et al., 2020). Copyright 2020, with permission from Elsevier.

Figure 1.7 (a) Optical images of typical carbon quantum dots illuminated under a white light (left, daylight lamp) and UV light (right, 365 nm). (b) Relationship between the carbon quantum dots size and bandgap energy. Reprinted with permission from (Li et al., 2010). Copyright 2010 American Chemical Society.

Figure 1.8 (a) Surface passivation of carbon quantum dots with diamine-terminated oligomeric polyethylene glycol (PEG1500N). (b) Strong photoluminescence of passivated carbon quantum dots. Reprinted with permission from (Sun, 2006). Copyright 2006 American Chemical Society.

Figure 1.9 Schematic representation of the products obtained at different hydrothermal temperatures. Used with permission of Royal Society of Chemistry, from (Song et al., 2015); permission conveyed through Copyright Clearance Center, Inc.

Figure 1.10 Solvothermal schematic of the synthetic process for the carbon quantum dots and inkjet printing. Reprinted with permission of *Chemistry Select* from (Deng et

List of Abbreviations

QDs quantum dots

CQDs carbon quantum dots

WS wheat straw

BR bamboo residue

QY quantum yield

UCPL up-conversion luminescence

PEG polyethylene glycol

UYTMs urchin-like and yolk-shell TiO2 microspheres

PL photoluminescence

HRTEM high resolution transmission electron microscopy

UV ultraviolet

CA citric acid

EDA ethylenediamine

1 Introduction

1.1 Potential applications and economic impact

1.1.1 Properties and applications of carbon quantum dots

1.1.1.1 Quantum dots

Fluorescence probes are among the most widely used imaging tools in biomedical research. With the rapid development of nanotechnology, fluorescent nanomaterials with excellent properties continue to emerge. Compared with traditional organic dyes, fluorescent nanomaterials have the advantages of high photostability, tunable emission spectra, and high quantum yield (QY) (Loukanov et al., 2016; Xu et al., 2016). Among many fluorescent nanomaterials, quantum dots (QDs) with unique photophysical properties and high QY have potential applications in bioimaging, sensing, catalysis, and other fields, as shown in **Figure 1.1**. QDs are initially defined as nanocrystals made of semiconducting materials, usually composed of group II-VI or III–V elements of the periodic table, such as CdSe, with a particle size smaller than the exciton Bohr (Bawendi et al., 1990; Chan, 2002).

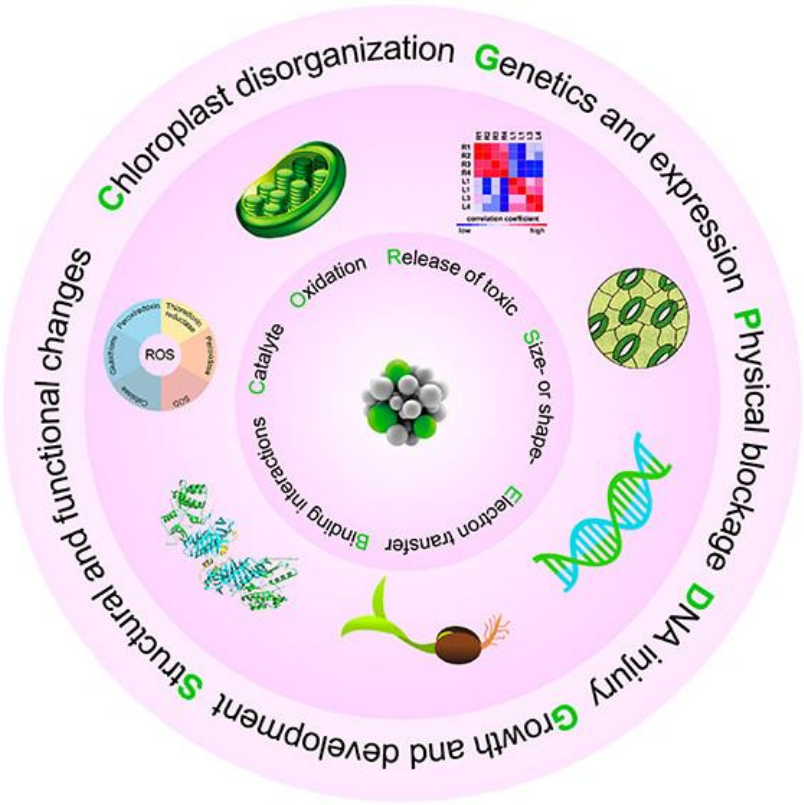

Figure 1.1 Properties and applications of semiconductor. Reprinted with permission from (Pang & Gong, 2019). Copyright 2019 American Chemical Society.

Compared to traditional and commonly used organic dyes, semiconductor QDs present obvious advantages as fluorescent probes, owing to their optical properties (Arul et al., 2017; Nair et al., 2020). Firstly, semiconductor QDs have broad excitation and narrow emission wavelength ranges, meaning that any wavelength smaller than the emission wavelength can be used. Thus, QDs are excited by the excitation light wavelength, and their fluorescence peak position can be regulated by changing their size. Moreover, QDs have a significant Stokes shift, which can avoid the overlap of the emission and excitation spectra, thereby allowing spectroscopic detection at low

signal intensities. In addition, the emission peaks of QDs are narrow and symmetrical, with a slight overlap and minimal mutual interference, which overcome the problems caused by spectral overlap. The emission wavelength of QDs can be adjusted by controlling their size and composition, thereby allowing the arbitrary synthesis of QDs that emit the desired wavelengths. Furthermore, QDs also have strong anti-photobleaching ability and high photochemical stability, which is approximately 100 times that of ordinary fluorescent dyes. Photobleaching refers to the phenomenon that reduces the fluorescence intensity by the decomposition of luminescent substances caused by light excitation. Finally, the luminescence lifetime of QDs is longer. However, semiconductor QDs face toxicity problems because of the presence of heavy metals, such as Cd, Hg, Zn, and Pb, thereby suspending clinical studies on them. Even at low doses, they tend to exert a harmful effect on human beings and the environment because of the heavy metals in their preparation. Such limitations prompt further development of QDs (Arul et al., 2017; Nair et al., 2020; Pang & Gong, 2019).

1.1.1.2 Carbon quantum dots

Carbon quantum dots are zero-dimensional carbon nanoparticles that have a size of smaller than 10 nm (Sun, 2006). Carbon quantum dots were accidentally first discovered in 2004 when Xu separated single-walled carbon nanotubes using gel electrophoresis from the carbon soot produced by arc discharge (Xu X, 2004).

Compared with traditional organic dyes and semiconductor QDs, carbon quantum dots

have excellent properties of non-toxicity, good biocompatibility, long luminescence lifetime, easy modification, good photostability, and good water solubility, resulting in their high potential for various applications (Loukanov et al., 2016; Younis et al., 2020). The most prominent property of carbon quantum dots is their fluorescent properties, which have a narrow-band tunable emission and size-dependent photoluminescence (PL). In detail, when carbon quantum dots absorb light, some electrons migrate from the ground state to a higher excited energy state, thereby leaving a hole. When the electrons and holes meet, the electrons return to the ground state, which fills the holes and releases excess energy. The resulting light color is consistent with the energy difference between the excited and ground states of the electrons and the size of the carbon quantum dots. Thus, the energy levels of the electrons can be controlled to emit different colors. In general, smaller carbon quantum dots result in a larger bandgap and a larger gap between the valence and conduction bands (Loukanov et al., 2016; Younis et al., 2020). Therefore, higher energy is required for the excitation and release of electrons to return to their ground state, as depicted by the change of the emitted fluorescent color from red to blue as shown in **Figure 1.2**.

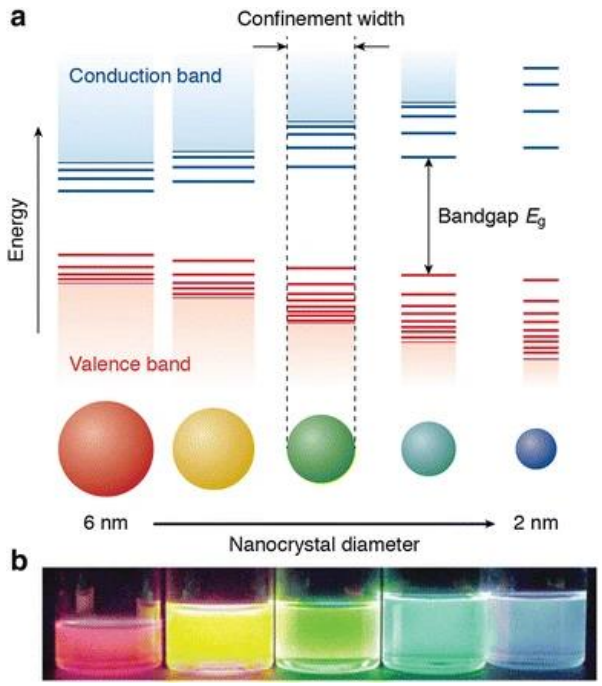

Figure 1.2 Schematic representation of the quantum confinement effect on the energy level structure of a semiconductor material. Used with permission of Royal Society of Chemistry, from (Donega´, 2011); permission conveyed through Copyright Clearance Center, Inc.

1.1.3 Carbon quantum dots applications

Traditional fluorescent nanomaterials, such as organic dyes and semiconductor QDs, have been used in various fluorescent applications owing to their strong and tunable fluorescence. However, the photobleaching and low extinction coefficients of organic dyes, poor water solubility and inherent toxicity of semiconductor QDs limit their safe use in clinical settings. Such drawbacks can be addressed using carbon quantum dots. Compared with traditional fluorescent nanomaterials, carbon quantum dots have good

water solubility, easy functionalization, low toxicity, high photobleaching resistance, and good biocompatibility, thereby exhibiting broad application prospects, as shown in **Figure 1.3** (Nekoueian et al., 2019; Pan et al., 2010; Xu et al., 2016; Younis et al., 2020; Zheng et al., 2015). Currently, carbon quantum dots have shown their strong potential in various applications, such as sensing (Molaei, 2020), biomedicine (Nekoueian et al., 2019; Pan et al., 2010; Xu et al., 2016; Younis et al., 2020; Zheng et al., 2015), and optoelectronic devices (W. Liu et al., 2020; Shaari et al., 2020; Wu et al., 2018; A. Xu et al., 2020; Yan et al., 2019; Yuan, 2016; Zhang & Yu, 2016; Zhang et al., 2012).

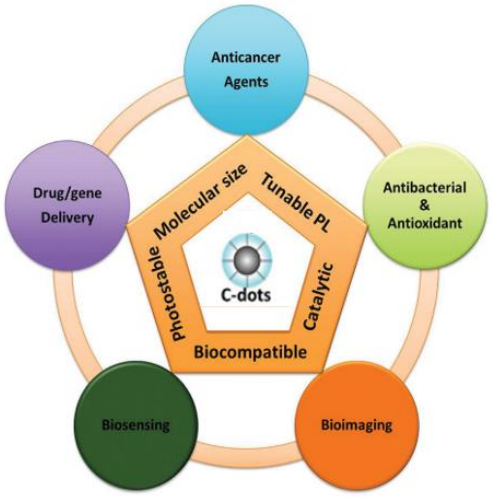

Figure 1.3 Carbon quantum dots applications. Reproduced with permission of *Small* from (Zheng et al., 2015). Copyright 2015 John Wiley and Sons.

In biological imaging, carbon quantum dots can replace traditional fluorescent nanomaterials as probes for early disease detection and cell imaging diagnosis.

Moreover, in biological therapy, carbon quantum dots can be used as cancer therapeutics and biomedical transporters for diseases, such as drug delivery, photodynamic therapy, and photothermal therapy.

In biological imaging, the most important hurdle that should be addressed is the absorption of almost all visible light wavelengths by imaging tissues and cells. In addition, the absorption of higher energy electromagnetic radiation (e.g., ultraviolet light) can damage the imaging target. Therefore, a narrow wavelength range of 650–900 nm is optimal for studying biological systems. Tao et al. (Tao et al., 2012) conducted the in vivo fluorescence imaging of carbon quantum dots injected into mice at different excitation wavelengths, with the optimal fluorescence contrast observed under an excitation of 595 nm. Huang et al. (Huang et al., 2019) mixed green renewable raw materials, namely wheat straw (WS) and bamboo residue, with urea to prepare amino-passivated carbon quantum dots by a one-pot hydrothermal method. The produced carbon quantum dots exhibit blue-green fluorescence and a QY of ~13% under an excitation of 365 nm. In vivo, optical imaging studies of the prepared carbon quantum dots were conducted by inoculating nude mice with tumor cells and subsequently intravenously injecting them with carbon quantum dots through the tail vein. Over time, the carbon quantum dots gradually accumulated in the kidney, liver, and tumor sites and displayed fluorescence, as shown in **Figure 1.4**, demonstrating the low toxicity and remarkable bioimaging performance of carbon quantum dots.

Furthermore, researchers have investigated the use of carbon quantum dots in biological imaging of various cells, including E. coli (Liu et al., 2009), Ehrlich ascites carcinoma cells (Ray, 2009), HeLa cells (Dong et al., 2012; Li, 2010; Pan et al., 2010), Hep G2 cells (Xu et al., 2013), LLC-PK1 (Hsu et al., 2012), NIH-3T3 fibroblast cells (Zhang et al., 2013), human lung cancer (A549) cells (Wu et al., 2018), T47D cells (Peng et al., 2012), murine alveolar macrophage cells (Wu et al., 2013), human hepatic cancer cells (Kumar et al., 2014), and MCF-7 cells (Dong et al., 2013).

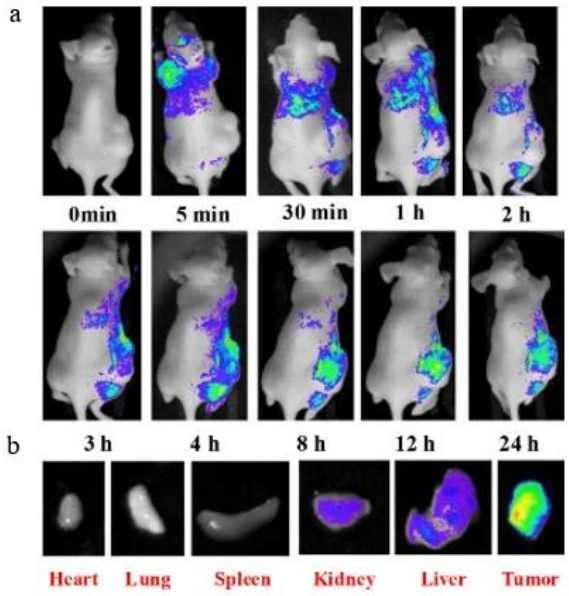

Figure 1.4 (a) In vivo fluorescence images of the mice after intravenous injection of the CQDs -WS solution. (b) Fluorescence images of the dissected mouse organ after intravenous injection of CQDs -WS solution for 1 day. Reprinted with permission of *Huang et al.* from (Huang et al., 2019); permission conveyed through Copyright Clearance Center, Inc.

Photocatalysis has recently gained significant attention. Traditional photocatalysts include titanium dioxide, zinc oxide, cadmium sulfide, and other oxide-sulfide semiconductors. However, the application of these catalysts is limited by their low light utilization and high photoinduced electron-hole complexation rates (Jiang et al., 2018). As functional nanomaterials with excellent optical and electronic properties, such as efficient light trapping, extraordinary up-conversion luminescence (UCPL), and excellent photoinduced electron transfer, carbon quantum dots are considered as effective components for constructing high-performance photocatalysts, which can broaden the photo response region and improve the separation rate of photoinduced charge carriers (Y. Liu et al., 2020; Yan et al., 2021). Guo et al. (Guo et al., 2019) synthesized carbon quantum dots through an electrochemical method and used them for decorating urchin-like and yolk-shell TiO_2 microspheres (UYTMs), as shown in **Figure 1.5**. The photocatalytic experiments were carried out by the photodegradation of aqueous phenol and methylene blue solutions. UYTMs with 2-8 wt.% carbon quantum dots have been studied, and the composite with 6 wt.% carbon quantum dots exhibited the highest photocatalytic efficiency with ~99% degradation rate of methylene blue after ultraviolet (UV) irradiation for 20 min. As the content of carbon quantum dots increases from 2 wt.% to 6 wt.%, the photocatalytic degradation efficiency is enhanced, mainly because carbon quantum dots with up-conversion properties can realize the conversion from partially visible light to near-ultraviolet light and promote the separation of photogenerated electron-hole pairs in the

heterojunction. However, when carbon quantum dots content increased to 8 wt.%, excessive carbon quantum dots tend to occupy the main active sites on the surface of TiO_2 and prevent the O_2 adsorption, resulting in a high recombination rate of electron-hole pairs and poor photocatalytic activity.

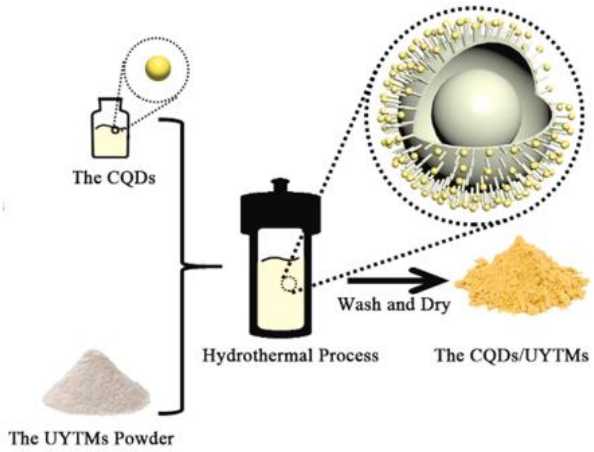

Figure 1.5 Formation process of the CQDs/UYTMs composites. Reprinted from (Guo et al., 2019). Copyright 2019, with permission from Elsevier.

In addition to TiO_2, other semiconductor photocatalysts have been combined with carbon quantum dots for applications in photocatalytic reactions, such as Bi-based compounds, CdS-based and graphitic carbon nitride composites. Wang et al. (Wang et al., 2020) synthesized carbon quantum dots by hydrothermal method and prepared CQDs/BiOBr. Their photocatalytic performance was evaluated by photodegrading bisphenol A. The efficiency of the resulting product significantly improved from 11.5% to 67.9% after introducing carbon quantum dots. This can be attributed to the broader

photo response region and improved separation ratio of the photoinduced electron-hole pairs after the introduction of carbon quantum dots. Huang et al. (Huang et al., 2020) produced a CQDs-modified composite CQDs@$CdIn_2S_4$/CdS using microwave-assisted method. The 1% CQDs@$CdIn_2S_4$/CdS composite was characterized by transmission electron microscopy (TEM) and high-resolution TEM (HRTEM), as shown in **Figure 1.6**. The prepared carbon quantum dots with up-conversion PL properties can convert light from a long wavelength ($\lambda > 600$ nm) to a short wavelength ($\lambda < 600$ nm). With the addition of 1 wt.%, the largest hydrogen evolution rate was obtained, which is 280 times that of commercially available P25. Thus, carbon quantum dots broadened the $CdIn_2S_4$/CdS composite light response range and improved its sunlight utilization. Di et al. (Di et al., 2020) prepared composite photocatalyst CQDs/g-C_3N_4 to degrade sulfamethoxazole. After 50 min of simulated sunlight exposure, the degradation rate of sulfamethoxazole by CQDs/g-C_3N_4 was ~97.3%, which was significantly higher than that of g-C_3N_4 (45.8%). This is ascribed to the role of carbon quantum dots as a donor-sensitizer-acceptor to facilitate charge separation and enhance light absorption.

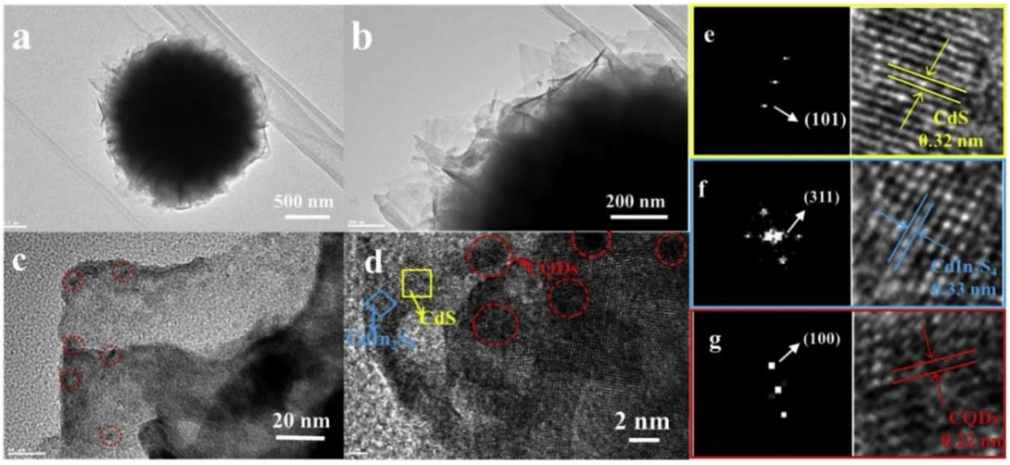

Figure 1.6 (a, b) TEM and (c, d) HRTEM images of 1% CQDs@$CdIn_2S_4$/CdS composites. HRTEM analysis results of (e) CdS, (f) $CdIn_2S_4$, and (g) Carbon quantum dots. Reprinted from (Huang et al., 2020). Copyright 2020, with permission from Elsevier.

1.1.2 Photoluminescence mechanism

PL is one of the unique properties of carbon quantum dots, along with narrow-band tunable emission, size-dependent PL, large absorption coefficient, size-dependent absorption, broad excitation spectrum, multiphoton excitation, easy functional grouping, good biocompatibility, good solubility in polar solvents, anti-photobleaching, no light flickering, good fluorescence stability, and low toxicity (Liu et al., 2019). Different PL properties and carbon quantum dots structures are obtained with the synthesis of varying reaction routes, conditions, and raw materials, resulting in difficulty studying their PL mechanism. Researchers have conducted extensive

studies on the PL properties of carbon quantum dots, including the different emission centers, excitation dependence, pH sensitivity and solvent sensitivity. Among them, emission centers of carbon quantum dots prepared by different methods have been extensively studied. Currently, three widely accepted PL mechanisms for carbon quantum dots are quantum confinement effect, surface state, and molecular state (Xu et al., 2016; Zhu et al., 2015).

1.1.2.1 Quantum confinement effect

The quantum confinement effect occurs when carbon quantum dots are smaller than their exciton Bohr radius (Chen et al., 2011). For carbon quantum dots with a perfect sp^2 graphene domain core and few surface chemical groups, the bandgap of the sp^2 graphene domain is considered the true intrinsic PL center of carbon quantum dots (Zhu et al., 2015). In other words, the PL emission of the carbon quantum dots can be tuned by adjusting the size of the sp^2 graphene domain, instead of the actual particle size (Ding et al., 2018). Typically, as the particle size decreases, the luminescence energies blue shift to a higher energy.

Li et al. (Li et al., 2010) used an electrochemical method to prepare carbon quantum dots with different particle sizes, as shown in **Figure 1.7**. To determine the PL emission center, the synthesized carbon quantum dots were treated with hydrogen plasma to remove the surface oxygen from the graphene surface. The result shows that no apparent change was observed in the PL spectra of the carbon quantum dots before

and after treatment, indicating that the PL center of the carbon quantum dots is the quantum-sized graphene structure itself rather than the carbon-oxygen surface. Furthermore, the PL properties were confirmed to vary with the particle size: 1.2 nm carbon quantum dots emit UV light, which is approximately 350 nm; 1.5–3 nm carbon quantum dots emit visible light in the range of 400–700 nm; 3.8 nm carbon quantum dots emit near-infrared light at approximately 800 nm. The particle size dependence is consistent with the quantum confinement effects. Similarly, Kim et al. (Kim, 2012) prepared carbon quantum dots of different sizes by cutting graphene oxide by the modified Hummers method. When the diameter of the carbon quantum dots were less than 17 nm, the absorption peak energy of the carbon quantum dots decreased with the increase in size and exhibited a red-shift emission owing to the quantum confinement effect.

Figure 1.7 (a) Optical images of typical carbon quantum dots illuminated under a white light (left, daylight lamp) and UV light (right, 365 nm). (b) Relationship between the carbon quantum dots size and bandgap energy. Reprinted with permission from (Li et al., 2010). Copyright 2010 American Chemical Society.

Carbon quantum dots are composed of light atoms with small dielectric constants and weak spin-orbit coupling, leading to strong carrier–carrier interactions and electronic states with well-defined spin multiplicity. Therefore, the energy band of carbon quantum dots is significantly larger than that of semiconductor QDs of similar size, resulting in the blue-to-green fluorescence color of most carbon quantum dots (Mueller et al., 2011).

1.1.2.2 Surface state

Surface states are determined by the hybridization of carbon skeletons and the attached chemical groups. Different functional groups have different energy levels, leading to a series of emission traps. Therefore, when the light of a specific excitation wavelength illuminates the carbon quantum dots, the surface state emission traps act as PL center. Higher degrees of surface oxidation or other effective modifications achieve more surface defects, leading to a red-shifted emission (Zhu et al., 2015).

Sun et al. (Sun, 2006) prepared carbon quantum dots by the laser ablation of a carbon target; however, no PL was detected. Then surface passivation was performed with polyethylene glycol (PEG). The passivated carbon quantum dots exhibit strong PL, as shown in **Figure 1.8**, which can be attributed to the surface energy wells.

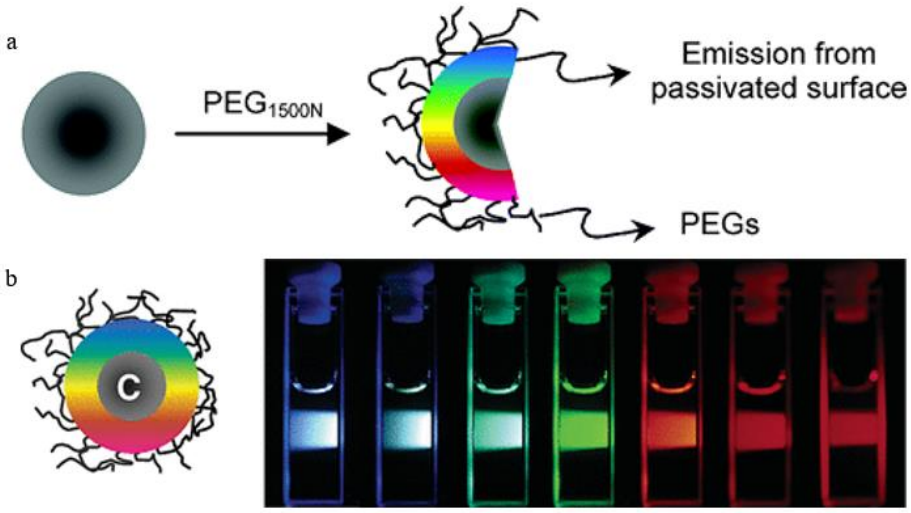

Figure 1.8 (a) Surface passivation of carbon quantum dots with diamine-terminated oligomeric polyethylene glycol (PEG1500N). (b) Strong photoluminescence of passivated carbon quantum dots. Reprinted with permission from (Sun, 2006). Copyright 2006 American Chemical Society.

1.1.2.3 Molecular state

Unlike the surface state formed by the synergistic hybridization of chemical groups and carbon cores, the molecular state is the PL center formed by organic fluorophores. The fluorophores formed at low reaction temperatures are attached to the surface or internal surface of the carbon skeleton and can directly exhibit PL emission. These exist only on the carbon quantum dots prepared by bottom-up route (Zhu et al., 2015).

Song et al. (Song et al., 2015) prepared carbon quantum dots from CA and EDA, as shown in **Figure 1.9**. At reaction temperatures of less than 150 °C, a type of bright

blue fluorophore 5-oxo-1, 2, 3, 5-tetrahydroimidazo [1,2-a] pyridine-7-carboxylic acid (IPCA) with a high QY was formed. At reaction temperatures of 150–250 °C, CA and EDA formed fluorophore molecules and a crosslinked polymer backbone. Carbon quantum dots were formed by the dehydration of CA and EDA. In this situation, the PL mainly results from the formed fluorophores connected to the carbon quantum dots. At high temperatures (over 300 °C), partial fluorophores are consumed to further form owing to further carbonization.

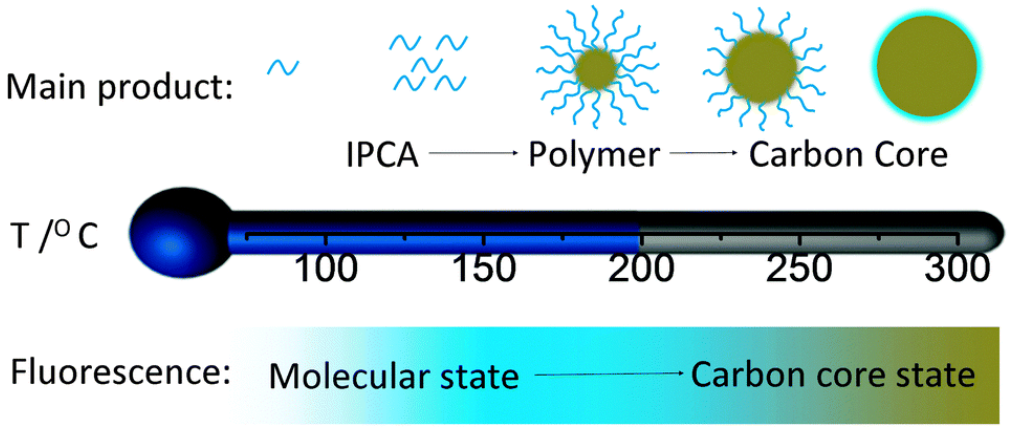

Figure 1.9 Schematic of the products obtained at different hydrothermal temperatures. Used with permission of Royal Society of Chemistry, from (Song et al., 2015); permission conveyed through Copyright Clearance Center, Inc.

1.1.3 Synthetic routes of carbon quantum dots

Currently, a wide variety of synthetic methods have been developed to produce carbon quantum dots, which are classified in two categories: top-down and bottom-up routes.

1.1.3.1 Bottom-up route

The bottom-up route produces carbon quantum dots from small precursors, such as carbohydrates and citrates, through hydrothermal (Li et al., 2020; Newman Monday et al., 2021; Ran et al., 2020), solvothermal treatments (Li et al., 2020), microwave-assisted (Gul et al., 2020) and ultrasonic-assisted methods (Saikia et al., 2019).

Monday et al. (Newman Monday et al., 2021) prepared EDA and L-phenylalanine-doped N-CQDs from natural abundant waste palm kernel husk by hydrothermal methods. The prepared carbon quantum dots exhibited an average particle size of 2 nm with a QY of 13.7% and 8.6% for the CQDs-EDA and CQDs-L-phenylalanine, respectively. Deng et al. (Deng et al., 2020) prepared carbon quantum dots by the solvothermal method using L-ascorbic acid as the carbon source, as shown in **Figure 1.10**. Under excitation at 365 nm, the aqueous solution of the carbon quantum dots emits fluorescence at 430 nm. Afterward, the carbon quantum dots were dissolved in a solvent mixed with polar solvent ethylene glycol and water in a volume ratio of 1:1 to prepare a fluorescent ink that meets the requirements of inkjet printing. Gul et al. (Gul et al., 2020) used banana peels to prepare carbon quantum dots by a microwave-assisted method. Carbon quantum dots with a particle size of 1.4 nm can be prepared in 5 min at 700 W. Carbon quantum dots emit blue fluorescence under 365 nm UV light. When Ag nanoparticles are incorporated into the carbon quantum dots matrix, they can be used as a colorimetric indicator probe for H_2O_2 and can also be applied to the detection of glucose oxidase. Saikia et al. (Saikia et al., 2019) oxidized anthracite

and bituminous coals with hydrogen peroxide under an ultrasonic bath, thereby forming carbon quantum dots in size range of 2–12 nm characterized by HRTEM, as shown in **Figure 1.11**. The method can be used as a simple large-scale synthesis of carbon quantum dots from abundant and economic coal resources for advanced applications. Although the bottom-up route offers high controllability and fewer product defects, the high cost of raw materials and poor water solubility of the resultant product are the main limitation (W. Liu et al., 2020; Manikandan & Lee, 2022; Younis et al., 2020).

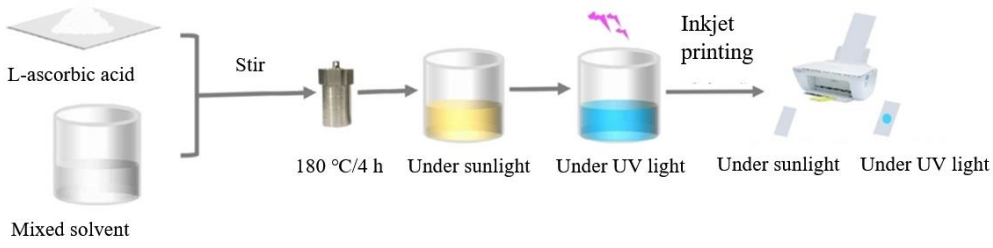

Figure 1.10 Solvothermal schematic of the synthetic process of the carbon quantum dots and inkjet printing. Reprinted with permission of *Chemistry Select* from (Deng et al., 2020). Copyright 2020 John Wiley and Sons.

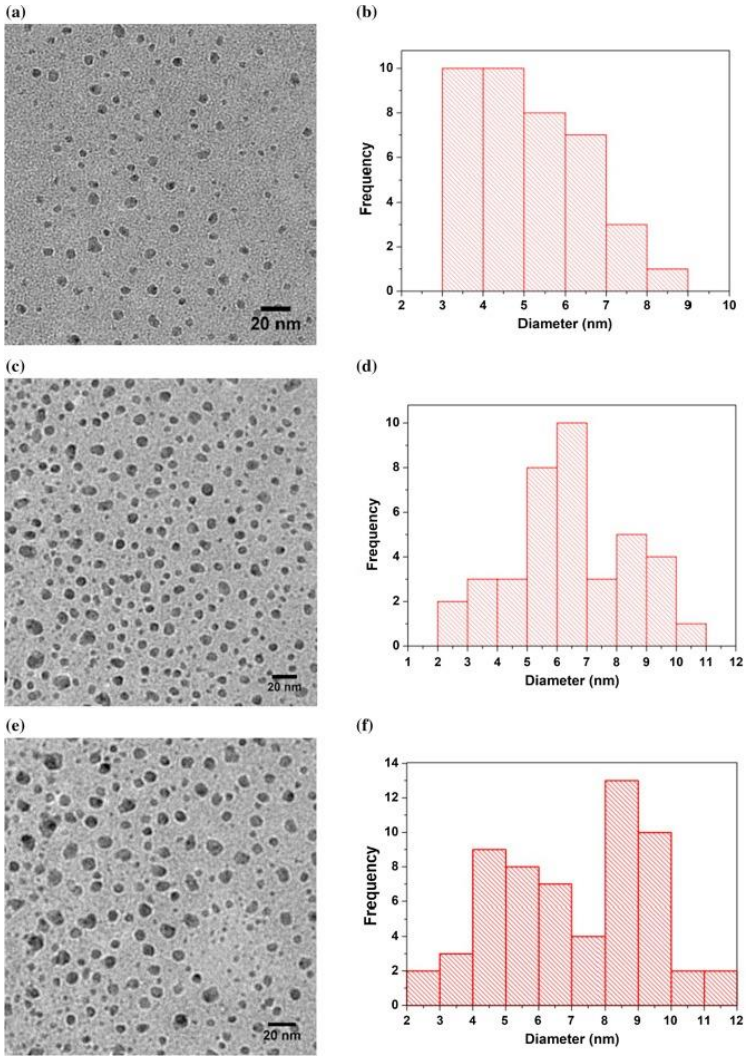

Figure 1.11 HRTEM micrographs of the carbon quantum dots (2–12 nm) at different magnifications (a, b) anthracite-produced carbon quantum dots, (c, d) semi-anthracite produced carbon quantum dots, and (e, f) bituminous blue gem coal produced carbon quantum dots. Reprinted from (Saikia et al., 2019), with permission from Elsevier.

1.1.3.2 Top-down route

The top-down route refers to breaking larger carbon structures, such as graphite powder, carbon fibers, and carbon nanotubes, into carbon quantum dots using

chemical oxidation (Qiao et al., 2010), laser ablation (Sun, 2006), arc discharge (Xu X, 2004), electrochemical (Li et al., 2011) and other technologies. The chemical oxidation method involves the exfoliation of precursor carbon materials, such as graphene oxide, carbon nanotubes, carbon fibers, and coal, by strong oxidizing agents and acids. This is a straightforward and cheap synthetic approach for the mass production of high-quality carbon quantum dots. Qiao et al. (Qiao et al., 2010) oxidized activated carbon with nitric acid to prepare carbon quantum dots with an average size of 4.5 nm, as shown in **Figure 1.12**(a). As-prepared carbon quantum dots exhibit good biocompatibility. After passivation with 4,7,10-trioxa-1,13-tridecanediamine or PEG_{1500N}, a QY as high as 12.6% was obtained. However, during the preparation of carbon quantum dots using strong acids, toxic gases are often released, resulting in impurities in the sample. This increases the production cost, since more labor is required to completely remove the excess acid or salt, thereby limiting the application of this method. Calabro et al. (Calabro et al., 2018)) used carbon nano-onions as the carbon source and ablated them under 1.30 W laser for 7 h to prepare carbon quantum dots with a size of 1.8 nm, as shown in **Figure 1.12**(b). Compared with the carbon quantum dots prepared by chemical oxidation, the surface functional group is the main emission center of the carbon quantum dots prepared by laser ablation. As their surface has more hydroxyl groups and due to its smaller size, a higher surface-to-volume ratio of the functional groups is obtained, resulting in a blue shift of the emission.

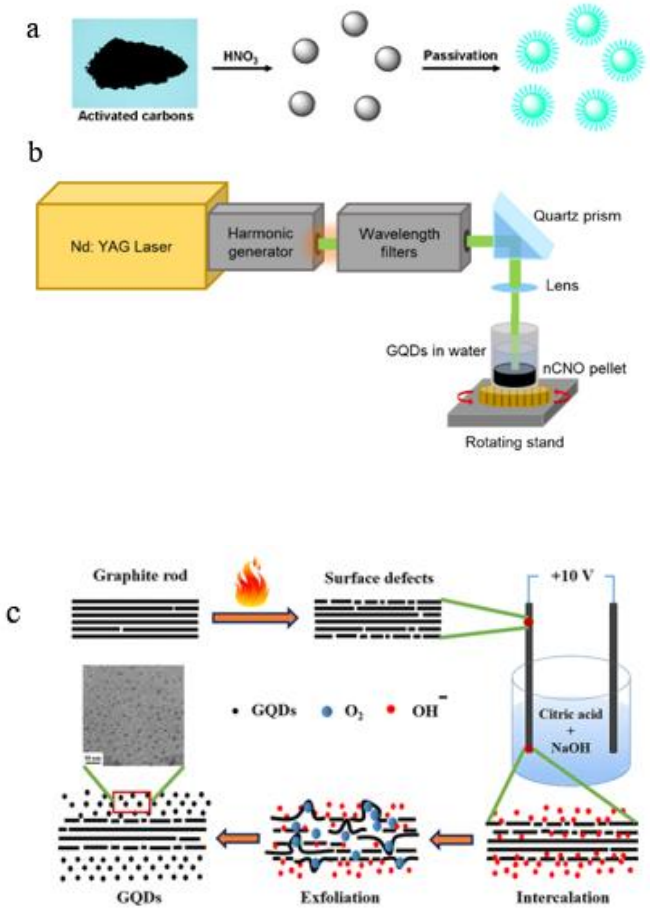

Figure 1.12 (a) Schematic illustration of the chemical oxidation carbon quantum dots synthesis method. Used with permission of Royal Society of Chemistry, from (Qiao et al., 2010); permission conveyed through Copyright Clearance Center, Inc. (b) Schematic illustration of the laser ablation carbon quantum dots synthesis method. Reprinted from (Calabro et al., 2018). Copyright 2018, with permission from Elsevier. (c) Schematic illustration of the preparation of carbon quantum dots through electrochemical exfoliation of the defect-induced graphite rod. Reprinted from (Ahirwar et al., 2017); permission conveyed through Copyright Clearance Center, Inc.

Xu et al. (Xu X, 2004) first prepared carbon quantum dots by simultaneously obtaining fluorescent carbon dots when preparing single-walled carbon nanotubes by arc discharge soot. Ahirwar et al. (Ahirwar et al., 2017) reported the preparation of carbon quantum dots from graphite rods by electrochemical exfoliation, as shown in **Figure 1.12**(c). In detail, the graphite rod was first heated to cause several defects on the surface of the graphite rod, which is called defect-induced graphite rod. During the electrochemical stripping process, the defect site is cut and oxidized, whereby more defects promote the cutting and oxidation processes. In addition, the electrolyte is a mixture of CA and NaOH in water. The as-prepared carbon quantum dots have an average size of 2–3 nm and emit blue to green fluorescence when irradiated with a 365 nm UV light. The top-down route is highly suitable for mass production because of the abundant and low-cost raw materials and simple operations. However, the broad size distribution of the products is the main problem that restricts its development and should be solved urgently (W. Liu et al., 2020; Yan et al., 2019).

1.2 Size Distribution Problem

In quantum mechanics, bandgap is related to quantum size, and its energy is inversely proportional to size (Kwon et al., 2014; Sk et al., 2014; Yeh et al., 2016). Since the size of carbon quantum dots affects the bandgap, the optical properties of carbon quantum dots largely depend on size, and the synthetic carbon quantum dots with narrow size distribution are significant for expanding the application range.

Compared with other raw materials, coal has the advantages of low cost and presenting small crystalline carbon domains linked by weak carbon chains, as shown in **Figure 1.13**. Thus, coal is used as a raw material for preparing carbon quantum dots (Cai et al., 2020; Raj & Balachandran, 2020). The chemical oxidation method is facile and effective for extracting carbon quantum dots from coal. The small crystalline carbon domains with defects present in the coal can be extracted with the oxidation technique.

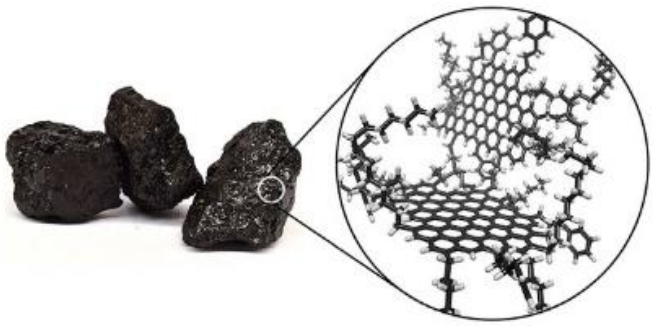

Figure 1.13 Macroscale image and simplified illustrative nanostructure of coal. Reprinted by permission from Springer Nature Nature Communications (Ye et al., 2013), copyright 2013.

Ye et al. (Ye et al., 2013) reported the synthesis of carbon quantum dots from different ranks coal using acidic oxidation technique with sulfuric and nitric acid, as shown in **Figure 1.14**. In this process, the area with graphene crystal area and sp^2 hybrid structure in coal can be extracted from the amorphous carbon with sp^3 hybrid structure

and other impurities by strong acid reagents. During exfoliation, the internal structure of the graphene crystal is not damaged; however, this synthetic method leads to the problem of the broad size distribution (Ye et al., 2013). To solve this problem, the mechanism of this method was analyzed, and subsequently, any contradictions were determined. The strength of the sp^2 and sp^3 covalent bonds within the graphene layers were ~524 and ~356 kJ/mol, respectively, whereas the van der Waals bonds between the graphene layers were only ~7 kJ/mol. The van der Waals bonds between the graphene layers is significantly smaller than the sp^3 covalent bonds in amorphous carbon. Therefore, we assumed that the sulfuric acid further destroyed the van der Waals bonds between the graphene layers.

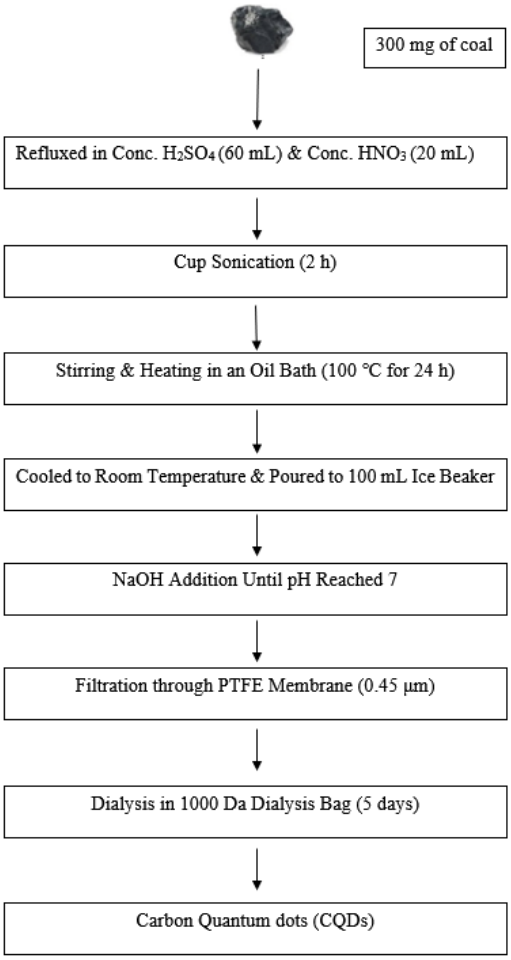

Figure 1.14 Synthetic procedure of carbon quantum dots from coal by Ye et al.

1.3 Previous Attempts

Although there have been studies trying to solve the problem of the broad size distribution, they have not started from the mechanism of chemical cutting, and the experimental method is limited by raw materials and operation. Ye et al. (Ye et al., 2015) explored the effects of temperature on the size distribution. The results showed

that smaller size and more narrow size distribution are obtained with a higher reaction temperature. Ye et al. (Ye et al., 2015) and Nilewski et al. (Nilewski et al., 2019) performed the cross-flow ultrafiltration method for size control. Zhang et al. (Zhang et al., 2019) and Yeh et al. (Yeh et al., 2016) used ultrafiltration through the membranes and gel electrophoresis, respectively. However, the additional post-treatment process increased the complexity of the operation and the experimental time. In addition, the researchers have used simulation method to study the process of sulfuric acid diffusion into the graphene layers. Seiler et al. (Seiler et al., 2018) simulated the process of sulfuric acid intercalation between graphite layers by Ab initio molecular dynamics simulation. The results showed that the ideal stacking of graphite layers and the presence of oxidants could effectively promote intercalation; on the contrary, inherent stacking faults will increase the free energy barrier, thereby hindering the intercalation process. However, the research is on regular graphite structures rather than coal structures. Thus, the root cause and scientific basis of the problems associated with the broad size distribution of coal carbon quantum dots should be determined to avoid blind trials without a mechanistic understanding.

1.4 Proposed plan

The purpose of the current research is to start the study on the exploration of the mechanism using dynamic simulation to explore the mechanism of carbon quantum dots synthesized from coal by sulfuric acid. Furthermore, we aim to address the

contradiction of whether concentrated acid can break the van der Waals bonds between the graphene layers. In addition, numerical simulation is more conducive to the detailed study of the reaction process to clarify the intermediate process of the reaction, thereby obtaining the size distribution of the intermediate products.

Therefore, we simulated the dynamic process to achieve size distribution control. In the process, sulfuric acid is inserted into the graphene layers in the reaction system, which destroys the van der Waals bonds. The larger the graphene layers, the longer it takes to destroy the interlayer van der Waals bonds. Within the 10000 iterations we performed, when graphene layers exceeded 5 nm, the van der Waals bonds between them could not be broken. The average size of bituminous powder crystal structure is 2.96 nm, the van der Waals bonds can be effectively broken, and a narrow size distribution can be obtained at the 1500th iteration, corresponding to the actual time of 34.2 h. However, because the average size of coke powder crystal structure is 5.8 nm, the van der Waals bonds cannot be effectively broken. Therefore, it cannot effectively break the van der Waals bonds, and narrow size distribution cannot be obtained through acid diffusion. The simulation results reveal the reason for the broad size distribution and provide guidance for the experimental operation, avoiding blind trials.

2 Methodology

Dynamic bond percolation model is intended to describe diffusion of small particles in a medium which is statistically disordered (Chang, 1993; Harris, 1986; Son & Wang, 2020; Xu, 1992). We used dynamic bond percolation model to simulate the diffusion of sulfuric acid between layers of the coal crystal structure.

2.1 Two-dimensional Model development

The destruction of coal particles by a sulfuric acid is a dynamic process. In this process, sulfuric acid molecular is inserted into the graphene layers in the reaction system, which destroys van der Waals bonds, as shown in **Figure 2.1**. In this process, it is challenging to intercalate the sulfuric molecule into the graphene layers because the distance between the graphene layers is only 0.35 nm. In comparison, the sulfuric molecule is about 0.39 nm. Thus, nitric acid is needed to deoxidize carbon atoms at the edge of graphene, and the graphene lamellar channel is opened and then diffused into graphene sheets by molecular thermal motion (Chen et al., 2022). Then, the intercalation interval is increased to 0.798 nm (Dimiev, 2012). Therefore, sulfuric acid diffusion process should be simulated.

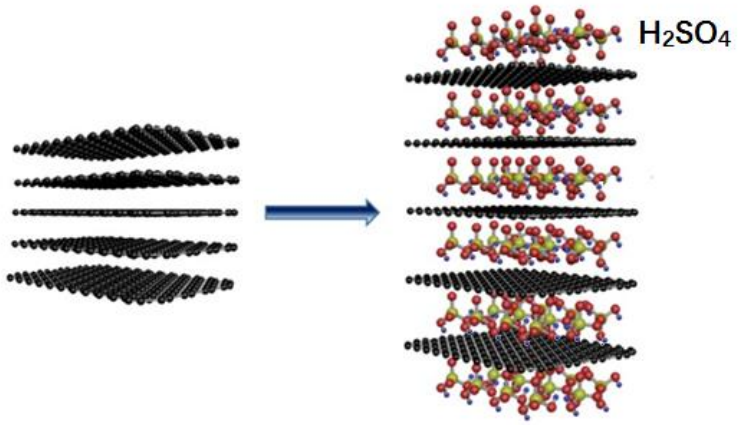

Figure 2.1 Insertion of sulfuric acid molecular into the graphene layers destroys the van der Waals bonds. Reprinted by permission from Springer Nature Nature Communications (Pei et al., 2018), copyright 2018.

Since there are many different ranks of coal in nature, such as bituminous and coke (Raj & Balachandran, 2020), we adjusted the size distribution of graphene crystal structure in the coal powder particles, simulated the acid diffusion process respectively, and analyzed the simulation results.

For the simulation, we created a two-dimensional (2D) 200 × 200 square along the X and Y axes for the simulation, where the x and y integers are in the range of 1 to 200, as declared in units of the spacing, as shown in **Figure 2.2**. We assume that the 200 × 200 square represents a part of the coal powder's cross-section, where the graphene crystal structure is surrounded by amorphous carbon. Red geometric figures represent graphene crystal in the coal particle, whereby its location, shape, and size are

randomly distributed in the square. Sulfate acid diffuse into the graphene layers, and the distance between the layers expands, resulting in the breakage of the van der Waals bonds between the layers.

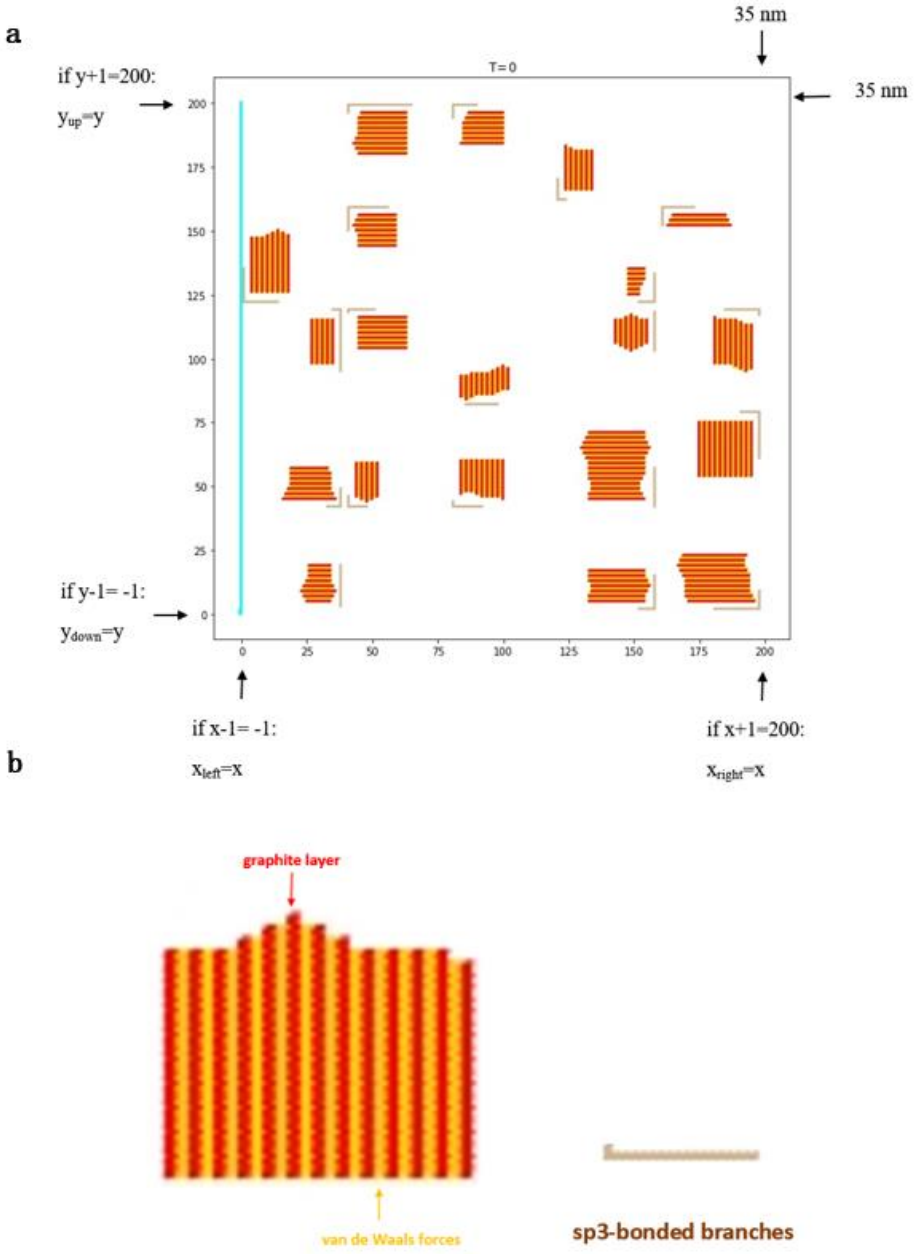

Figure 2.2 (a)2D 200 × 200 square model for sulfuric acid diffusion, corresponds to 35 nm×35 nm. Boundary conditions are shown. (b) The graphene layers, sp^3-bonded

branches, and van der Waals bonds are designated by red, brown, and yellow lines, respectively.

2.2 Diffusion Formula

The diffusion process is simulated according to the master formula (1) (Xu, 1992):

$$P_{new} = P_{old} + s\sum_{j}\left(P_j W_{ji} - P_i W_{ij}\right) \quad (1)$$

where P is the acid level, W is the diffusion path (de-binding), P_{new} is the updated P, P_{old} is the P that should be updated, P_i is the water level at site i, and j is the site adjacent to site i, including four sites up, down, left, and right.

In the square, each site is associated with a value of the acid level, represented by P, as shown in **Figure 2.3**. For example, site i is connected by the possible diffusion paths to its left, right, upper, and down. The diffusion path is represented by W, indicating the possibility of breaking the bond, and its values will be updated during the actual acid diffusion process.

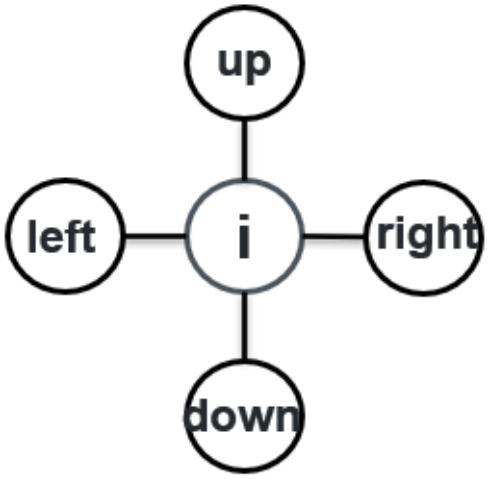

Figure 2.3 The possible diffusion paths to left, right, upper, and down of site i.

The master formula is derived from the following derivation process to obtain an updated P value:

$$P_{new} = P_{old} + dPi \tag{2}$$

Introducing Fick's Second Law:

$$\frac{\partial P}{\partial t} = D\frac{\partial^2 P}{\partial x^2} \tag{3}$$

where D is the diffusivity, 9.8×10^{-10} m^2/s (Leshin, 2004).

$$dPi = \frac{D \times dt}{dx^2}\sum_j \left(P_j W_{ji} - P_i W_{ij}\right) \tag{4}$$

where dt is the time step; and dx is the unit length, 0.175 nm.

Diffusivity variable *s* is then introduced:

$$s = \frac{D \times dt}{dx^2} \tag{5}$$

By introducing *s* into formula (3), master formula (1) is obtained.

In the coal particles, the graphene layers and sp^3-bonded branches are indicated by red and brown lines, respectively. As the graphene layers and sp^3 branches are not breaking, the P and W values are always equal to 0, indicating that they are non-penetrable. For the van der Waals bonds (yellow lines), W = 0.2 (Xu, 1992) for the start of the diffusion, which increases with the P value. For all sites, P =0 at the beginning, and W is randomly updated within [0,1] and multiplied by the diffusivity. In the diffusion model, the diffusivity path to the neighbor site is different, represented by the W value, indicating its difference from Fick's diffusion. The diffusivity bridging all sites are the same in Fick's diffusion.

Diffusion occurs by setting P = 1 at the left boundary, as shown in **Figure 2.2**, as indicated in the blue line at the left. When P reaches 1, coal breaks and is painted with blue color. When the whole yellow line turns blue, it indicates the van der Waals bonds have been broken, and it will be painted green.

To avoid the index being out of bounds, we apply boundary conditions, as shown in formula (6)-(9):

$$if\ x + 1 = 200: \quad x_{right} = x \tag{6}$$

$$if\ x - 1 = -1: \quad x_{left} = x \tag{7}$$

$$if\ y + 1 = 200: \quad y_{up} = y \tag{8}$$

$$if\ y - 1 = -1: \quad y_{down} = y \tag{9}$$

The final ideal result is that the yellow line becomes green when the acid level P reaches 1, which means the van der Waals bonds break, and the graphene layers are successfully stripped off, as shown in **Figure 2.4**.

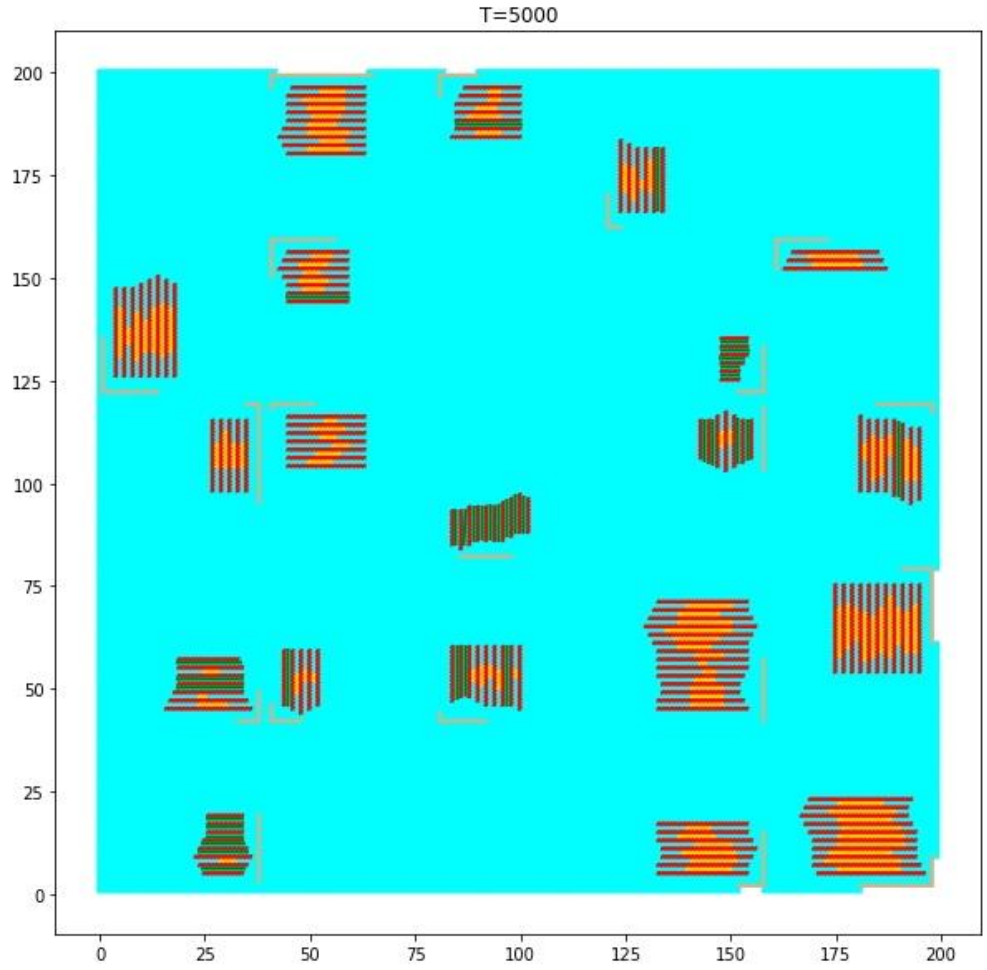

Figure 2.4 Final ideal result of sulfuric acid diffusion.

2.3 Programming Scheme

A block diagram of the programming is presented in **Scheme 1**.

The CPU running time of bituminous particles is 154.28 min, and the CPU running time of coke particles is 445.62 min.

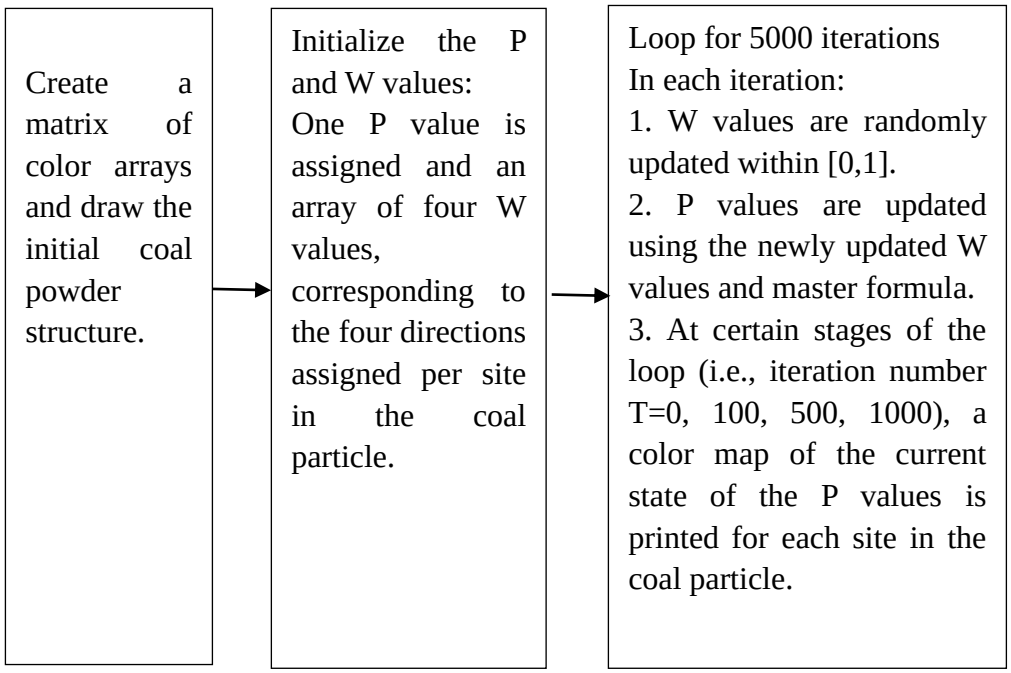

Scheme 1 Modeling process of the acid diffusion.

2.4 Quantification of acid diffusion

To quantitatively describe the process of acid diffusion over time and extraction of coal particles, the x coordinates were averaged using the P values via $<x^2>$, which is plotted against the time steps and is calculated by the formula (10):

$$< x^2 >= \sum P_i x_i^2 \qquad (10)$$

2.5 Size distribution statistics

Since carbon quantum dots products with a narrow size distribution will expand the

potential applications of carbon quantum dots, we statistically analyzed the size distribution of the carbon quantum dots products during the acid diffusion process.

The dimension measurement of carbon quantum dots at iteration number T=0, 1500, 2000, 2500, 3000, 4000 and 5000 are performed by Nano Measurer software. Snapshots of the acid diffusion were taken at iteration number T=0, 1500, 2000, 2500, 3000, 4000 and 5000, respectively. The interlayer size of graphene layers is set to 0.35 nm, as shown in **Figure 2.5**. Then, lines are drawn on the snapshots to measure the length and width of each geometric figure, as shown in **Figure 2.6**, calculate their area, and obtain their one-dimensional particle sizes according to the following formula (11):

$$N = \sqrt{A} \tag{11}$$

where N represents the one-dimensional particle size, and A represents the area of the geometric figure, which is calculated from the measured length and width.

One-dimensional particle size data of several diffusion process results were collected, and the Origin software was used for statistics. Particle size frequency histograms were generated, and Gaussian fitting was performed. Then, the particle size distribution was obtained, and the mean value and standard deviation were analyzed to obtain the ideal narrow size distribution.

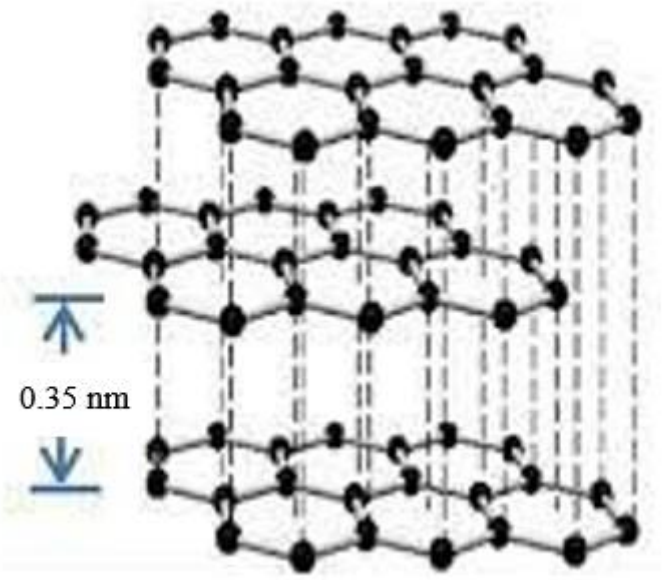

Figure 2.5 Graphene layer's structure.

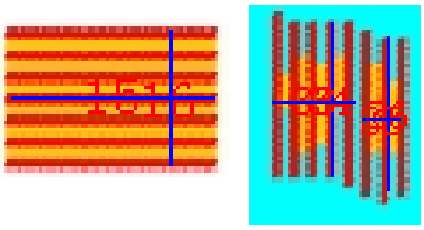

Figure 2.6 Length and width measured by Nano Measurer software. The blue lines are the length and width measurements.

3 Results and discussion

3.1 Diffusion results of bituminous particle

We created a two-dimensional square to simulate the sulfuric acid diffusion in the graphene particle and the breakage of the van der Waals bonds between the graphene layers. **Figure 3.1-3.4** shows the snapshot of the diffusion process at iteration number T=0, 100, 750, 1500, 2000, 3000, 4000 and 5000, when diffusivity variable s = 0.44, and dt=1.35×10^{-11} sec. By setting P=1 at the left boundary, diffusion occurs. The graphene layers, sp^3-bonded branches, and van der Waals bonds are indicated by the red, brown, and yellow lines, respectively. The blue sites represent the areas with P = 1, and the green line represents the van der Waals bonds that have been successfully broken.

We simulate the acid diffusion process of bituminous particles. The proportion of crystal structure in the simulated bituminous particles is 13%. At T=1500, the van der Waals bonds started to break, and some small graphene layers were peeled off. At T=5000, the graphene layers were successfully peeled off. Therefore, an ideal peeling result was obtained, which suggests that the sulfuric acid can effectively break the van der Waals bonds and peel off the graphene layers.

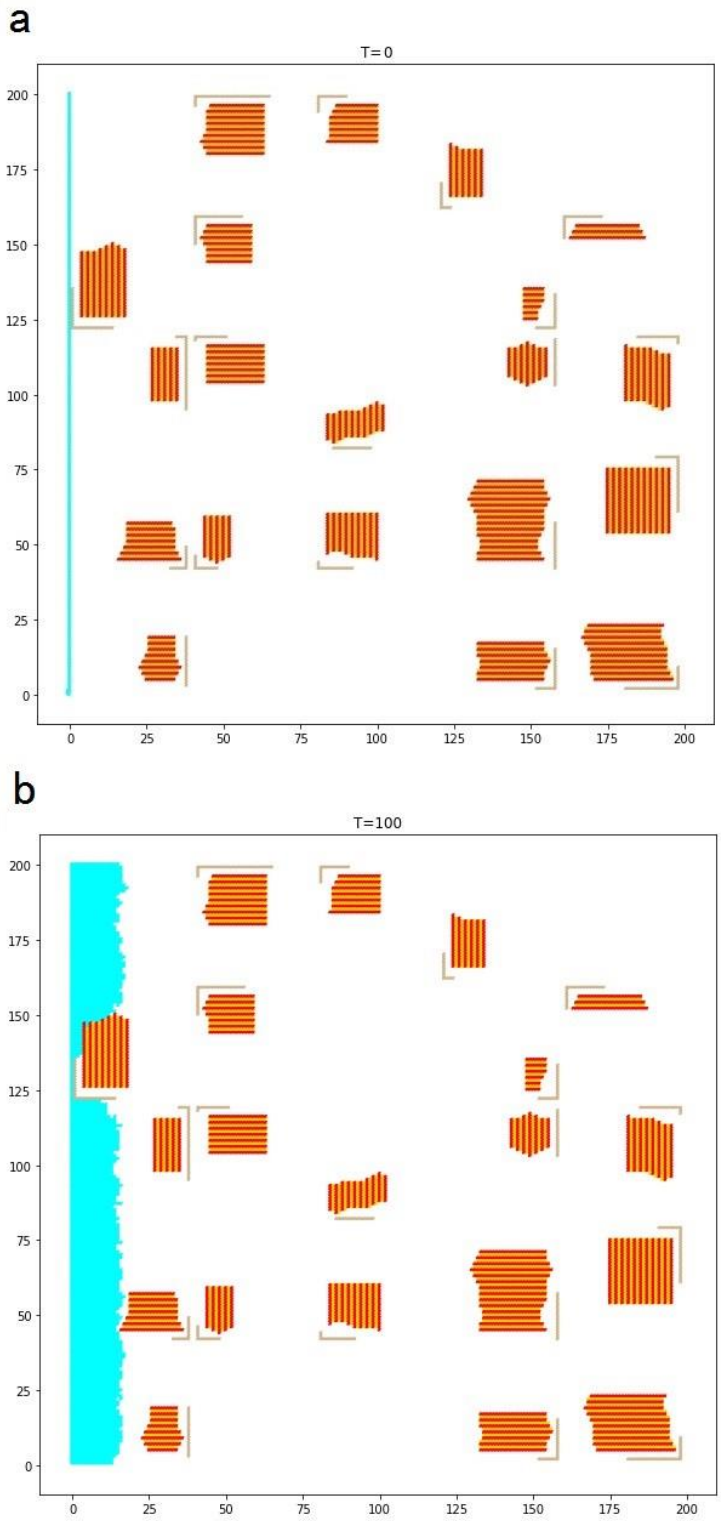

Figure 3.1 Snapshot of the bituminous particles diffusion process at iteration number (a) T=0, (b) T=100.

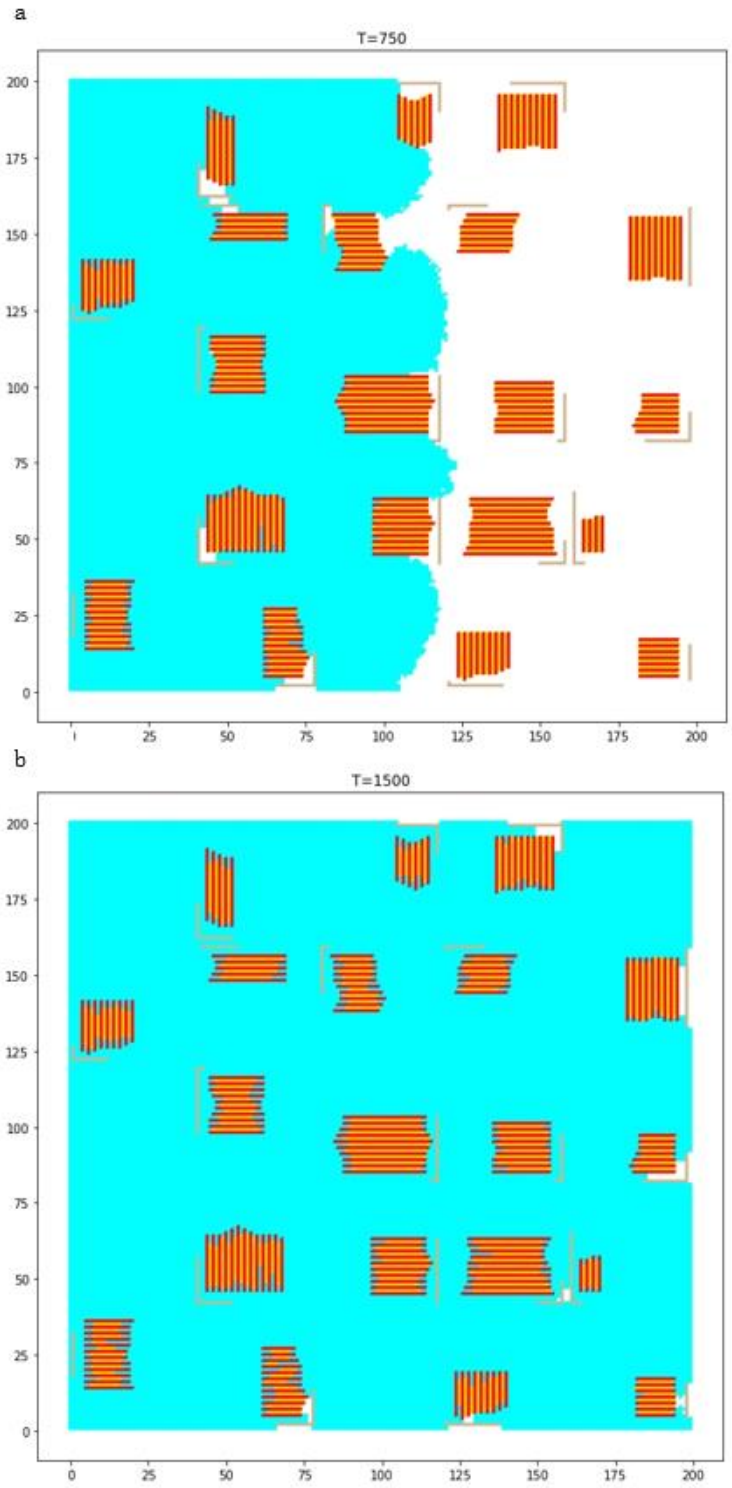

Figure 3.2 Snapshot of the bituminous particles diffusion process at iteration number (a) T=750, (b) T=1000.

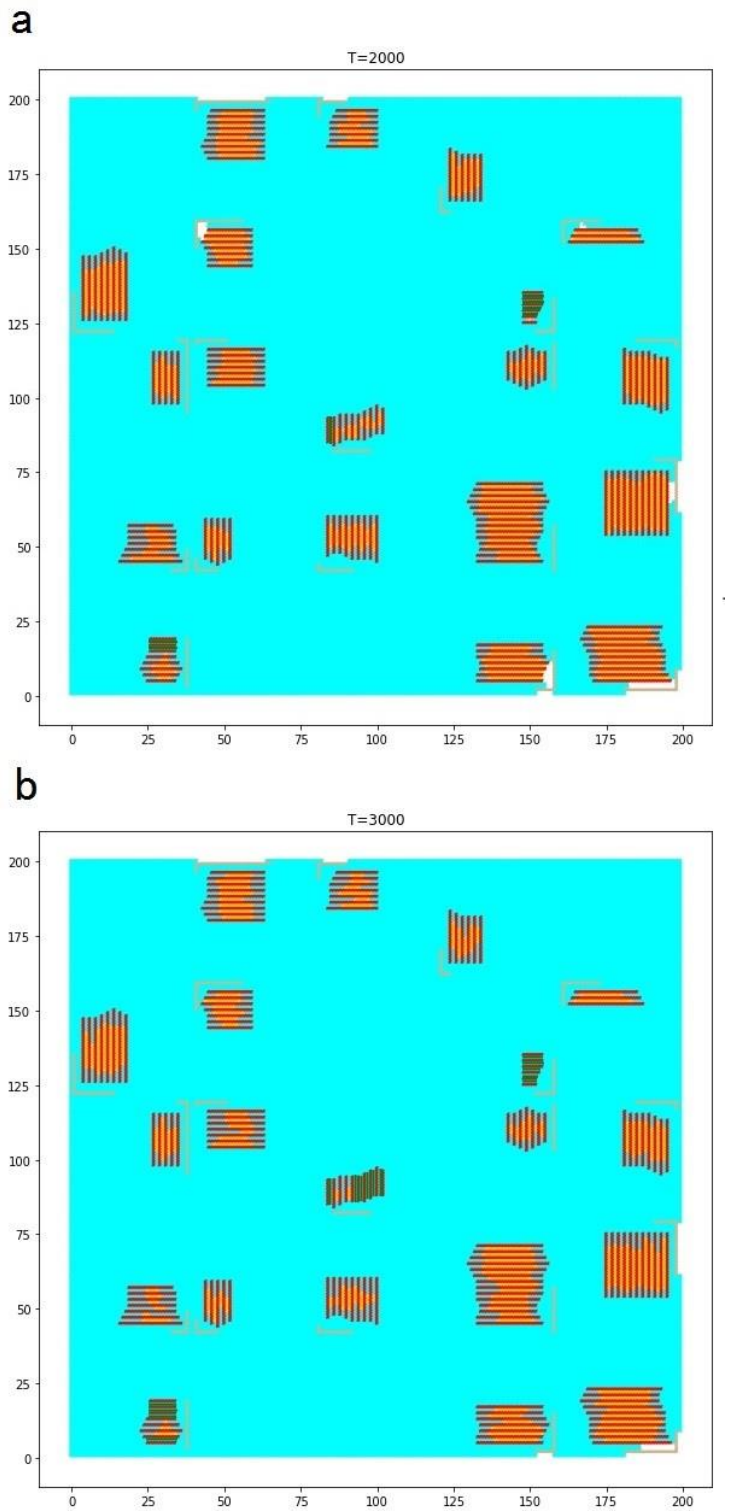

Figure 3.3 Snapshot of the bituminous particles diffusion process at iteration number (a) T=2000, (b) T=3000.

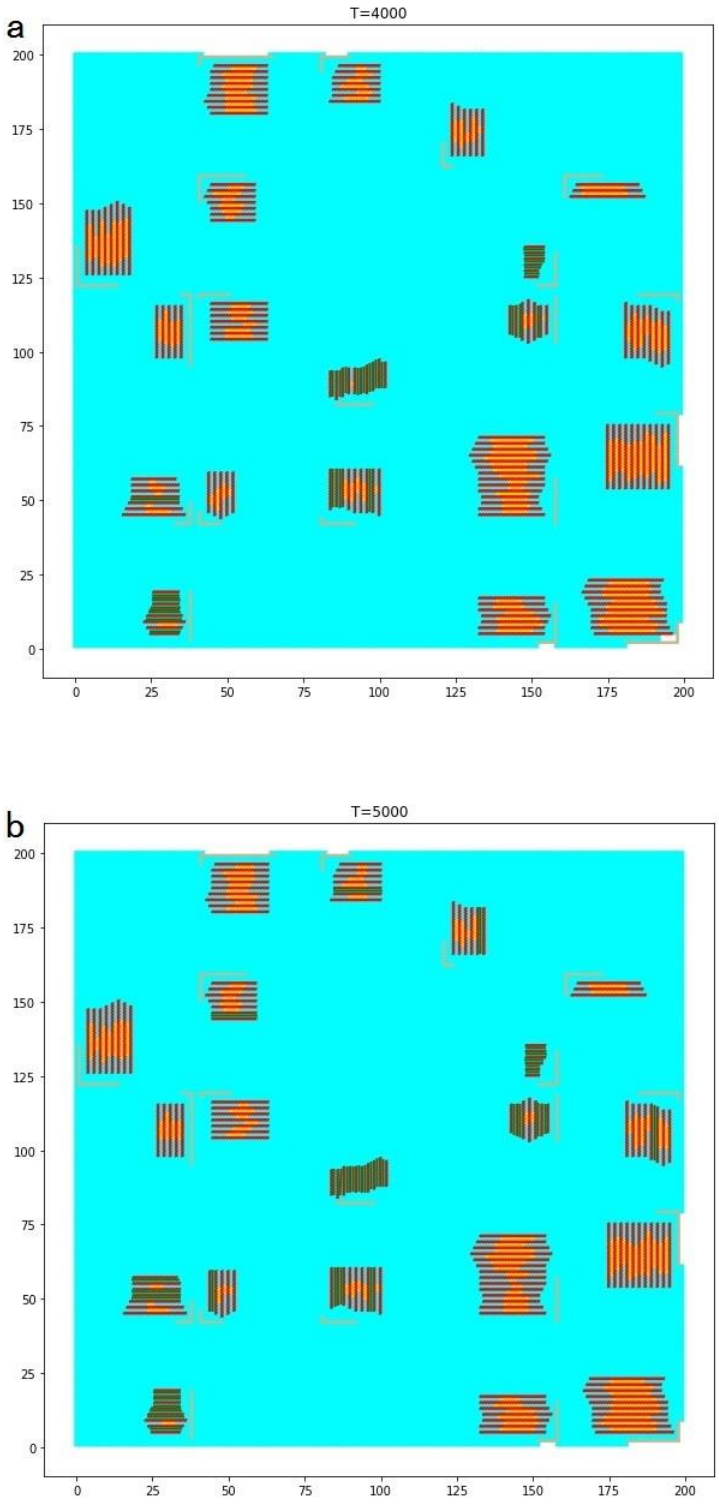

Figure 3.4 Snapshot of the bituminous particles diffusion process at iteration number (a) T=4000, (b) T=5000.

3.2 Quantification of acid diffusion

To quantitatively describe the process of acid diffusion over time and extraction of coal particles, the x coordinates were averaged using the P values via $<x^2>$, which is plotted against the time steps. When diffusivity variable *s* = 0.44, and dt=1.35×10^{-11} sec, a complete diffusion curve was obtained within 5000 iterations, as shown in **Figure 3.5**. When the *s* value was decreased to 0.2, the diffusion process is excessively slow, and a complete diffusion curve cannot be obtained within 5000 iterations. When diffusivity variable s is excessively large by 0.7, the curve diverges, as shown in **Figure 3.6**.

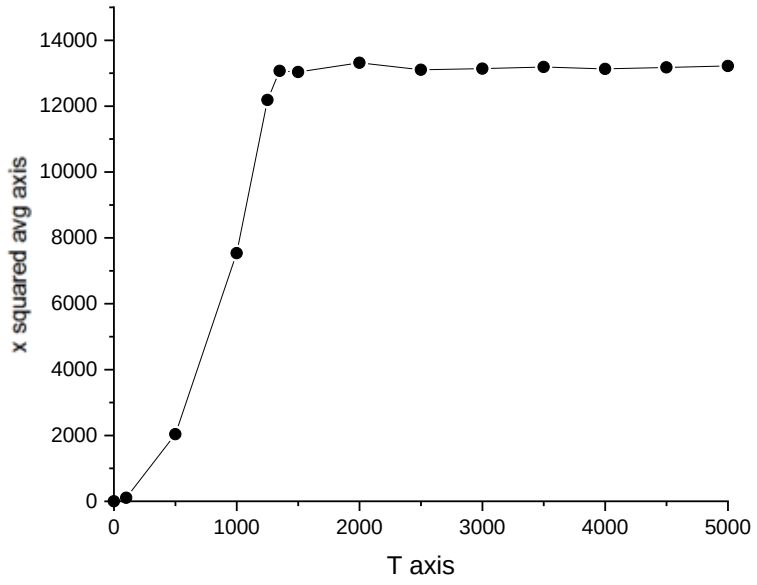

Figure 3.5 Diffusion curve $<x^2>$-t of bituminous particle when diffusivity variable *s* = 0.44.

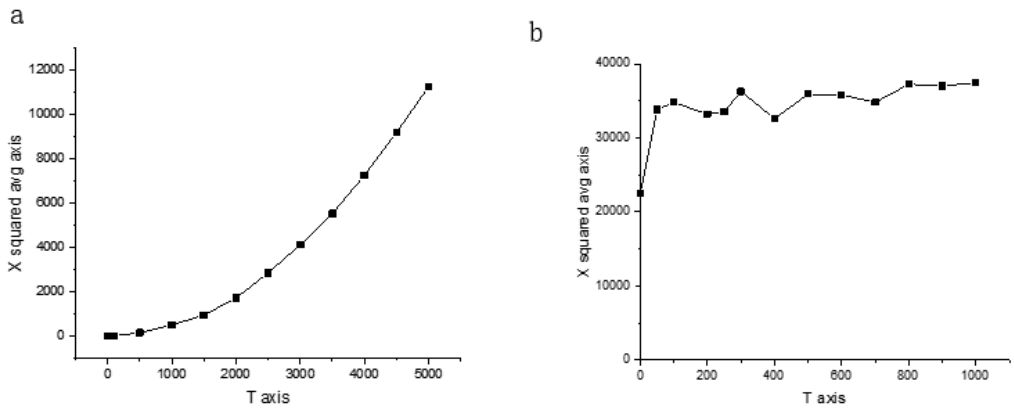

Figure 3.6 Diffusion curve $<x^2>$-t of bituminous particles when diffusivity variable (a) s = 0.2 and (b) s = 0.7.

According to previous studies (Ye et al., 2013), sulfuric acid is able to exfoliate the amorphous carbon around the graphene crystal structure to obtain carbon quantum dots, as confirmed by our simulation. From bituminous particle simulation results, we believe that by extending the experimental time, sulfuric acid can further destroy the van der Waals bonds between the layers, thereby peeling off the graphene layers and obtaining carbon quantum dots with a controllable size.

3.3 Bituminous particle size distribution results

To expand the application range of carbon quantum dots, we explored obtaining carbon quantum dot products with a narrow size distribution. Therefore, we made statistics on the size distribution of the acid diffusion process of bituminous particles.

For bituminous particles, diffusivity variable *s*=0.44, it was found that the graphene layers began to peel off at the 1500th iteration, so made statistics on the size distribution of the acid diffusion process at the 0th, 1500th, 2000th, 2500th, 3000th, 4000th and 5000th iterations, as shown in **Figure 3.8-3.12**. According to Ye et al. (Ye et al., 2013) result, bituminous graphene crystal structure size distribution is 2.96± 0.96 nm, as shown in **Figure 3.7.** Therefore, at the 0th iteration, we made similar size distribution, which is 2.64±0.87 nm, as shown in **Figure 3.8.** At the 1500th iteration, the size distribution becomes to 2.71±0.51 nm, because some small-sized graphene layers start to peel off. Between the 2000th to 2500th iteration, more graphene layers are peeled off, resulting in the formation of two peaks at 0-0.5 nm and 2.5-3 nm, and the size distribution does not conform to the Gaussian distribution. However, larger-sized particles can be separated by centrifugal or dialysis methods; therefore, we made statistics for the size distribution of particles larger than 1 nm, which are 2.59±0.74 nm and 2.64±0.83 nm, respectively. At the 3000th, 4000th and 5000th iterations, the size distribution is 0.56±0.29 nm, 0.58±0.34 nm, and 0.69±0.25 nm, respectively. During this process, larger graphene layers are exfoliated, and the size distribution peak shifts from 0-0.5 to 0.5-1 nm, resulting in a slight increase in size distribution. The narrow size distribution was obtained at the 5000th iteration.

In order to make the simulation results have a guiding value for the actual experiment, we convert the simulation time into the actual experiment time. For 35 nm×35 nm

particles, the actual time corresponding to 5000 iterations is 6.75×10^{-8} sec. According to Fick's second law, diffusion time is proportional to the square of the diffusion distance, as shown in formula (3). The particle size of the actual bituminous raw material used by Ye et al. (Ye et al., 2013) in the experiment is 110 μm. 2D simulation starts the diffusion from one side, in actual particles, the diffusion progresses from one side to the middle and therefore the size increases to 55 μm×55 μm. The actual time to obtain narrow size distribution at the 5000th iteration is 114 h, which is much larger than experiment time 26 h (Ye et al., 2013). To obtain a narrow size distribution in a shorter time, the 1500th iteration is the subsequent narrowest size distribution, corresponding to 34.2 h. Therefore, in the actual experiment process, at the reaction time of 34.2 h, the carbon quantum dot products with narrow size distribution can be obtained after separation using centrifugation and dialysis methods.

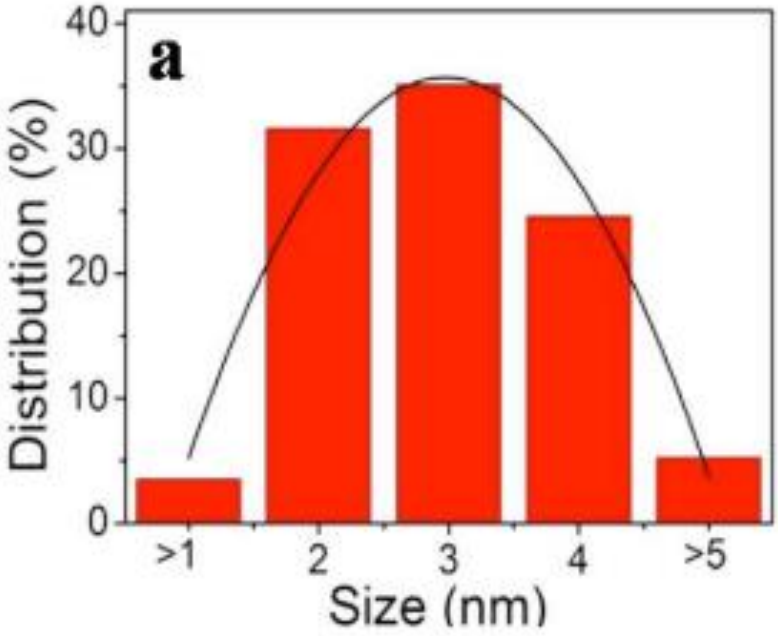

Figure 3.7 Ye et al. bituminous carbon quantum dots size distribution, size=2.96± 0.96 nm. Reprinted by permission from Springer Nature Nature Communications (Ye et al., 2013), copyright 2013.

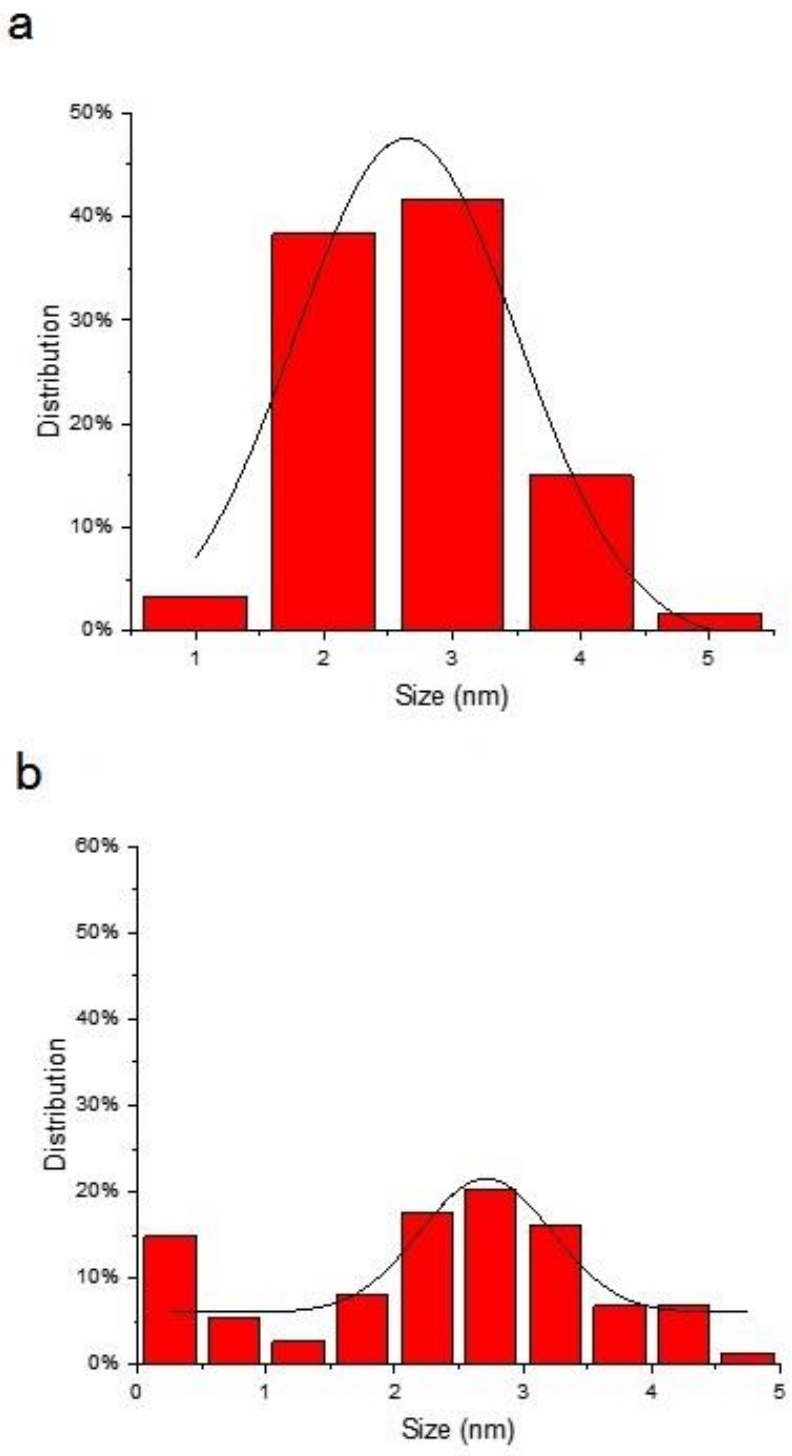

Figure 3.8 Bituminous carbon quantum dots size distribution at (a) T=0, size=2.64± 0.87 nm; (b) T=1500, size=2.71±0.51 nm.

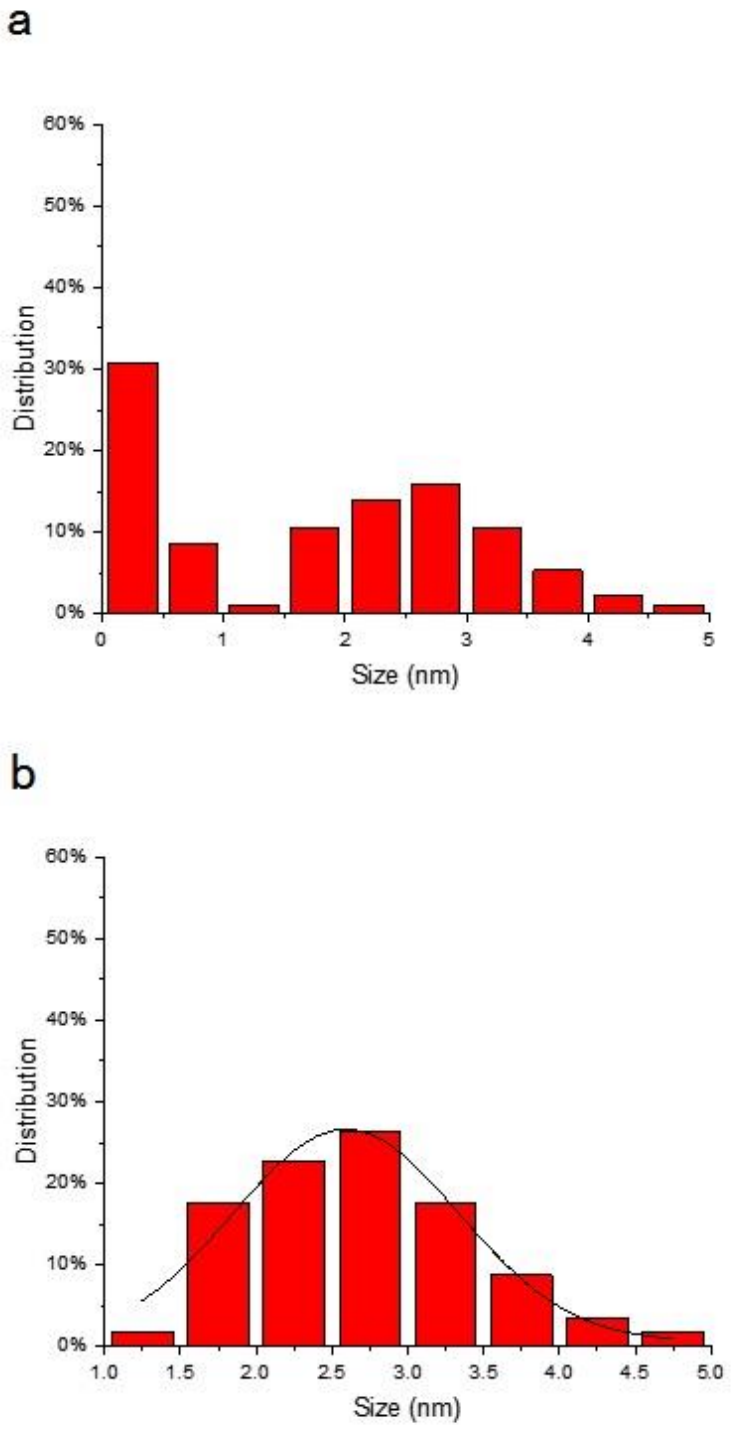

Figure 3.9 Bituminous carbon quantum dots size distribution at (a) T=2000; (b) size distribution larger than 1 nm, size=2.59±0.74 nm.

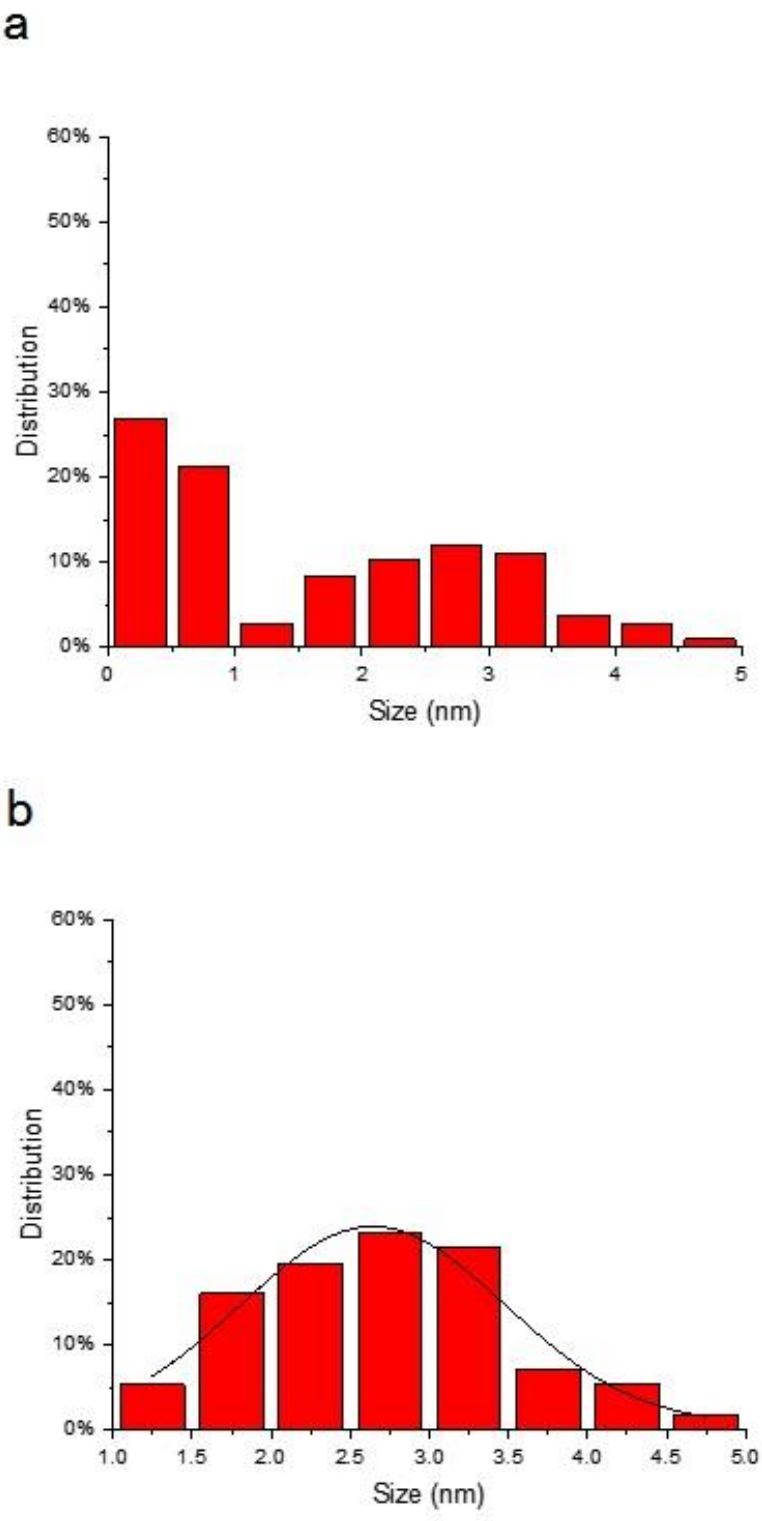

Figure 3.10 Bituminous carbon quantum dots size distribution at (a)T=2500; (b) size distribution larger than 1 nm, size=2.64±0.83 nm.

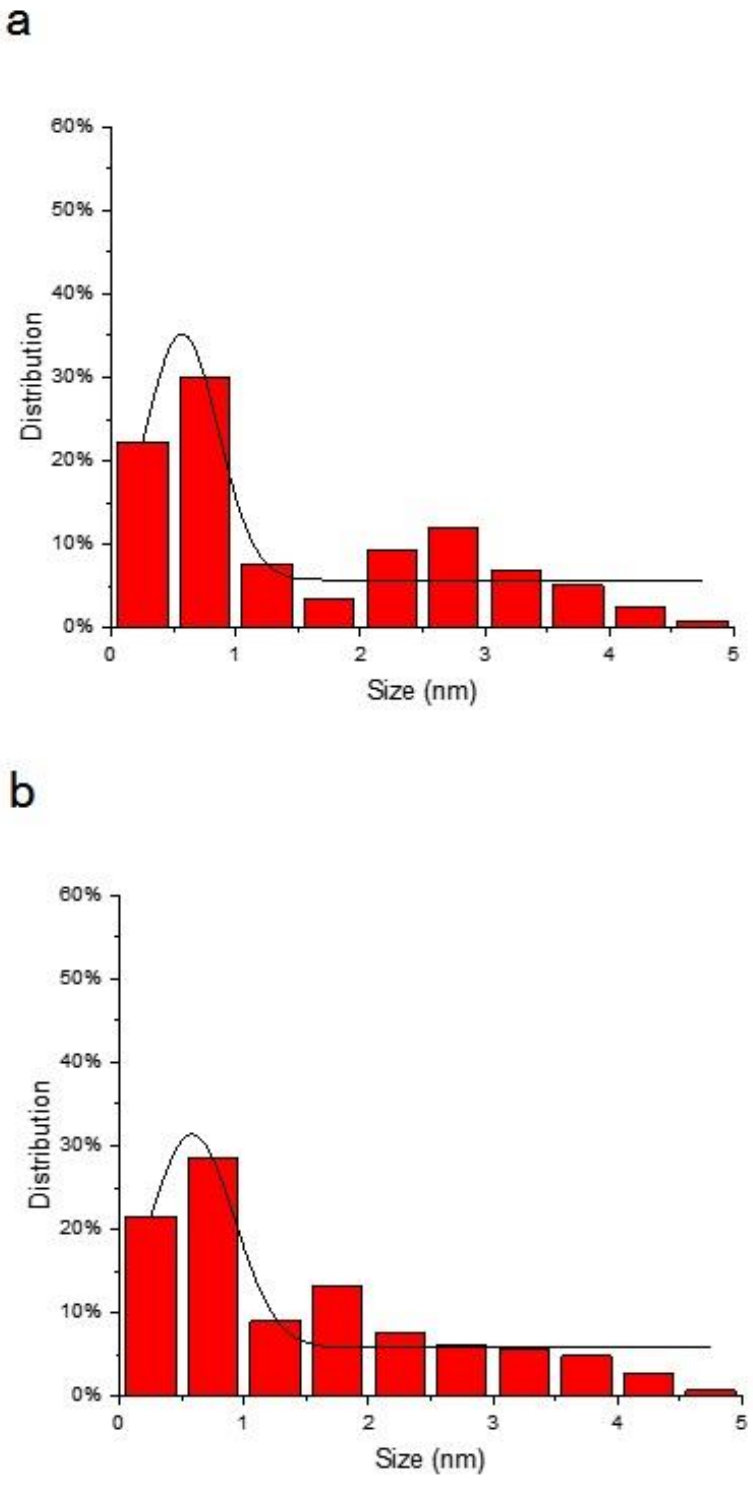

.

Figure 3.11 Bituminous carbon quantum dots size distribution at (a)T=3000, size=0.56±0.29 nm; (b) T=4000, size=0.58±0.34 nm.

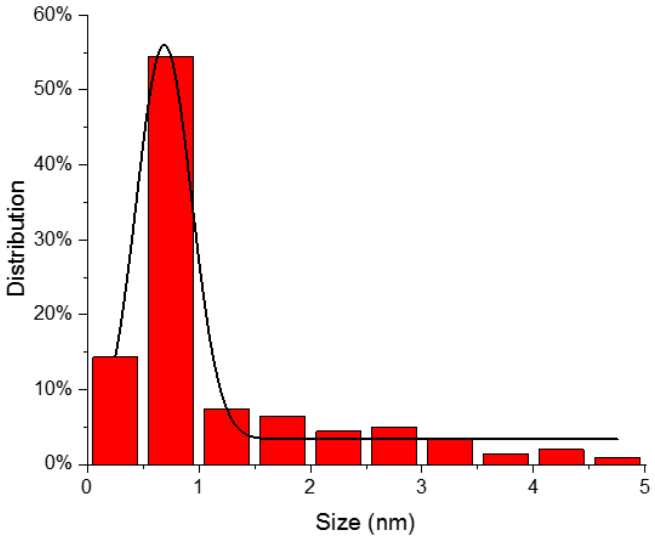

Figure 3.12 Bituminous carbon quantum dots size distribution at T=5000, size=0.69 ±0.25 nm.

3.4 Diffusion results of coke particle

Since there are many different ranks of coal in nature, such as anthracite, bituminous, and coke, we adjusted the graphene crystal structure size distribution in the coal powder particles, simulated coke particle acid diffusion, and analyzed the simulation results.

To simulate coke particles, we increase the 2D model to 350×350, corresponding to the actual size of 61.25 nm×61.25 nm, and increase the iteration number to 10000, the proportion of crystal structure in the simulated coke particles is 17%, as shown in **Figure 3.13-3.16**. In diffusion process, s=0.44, and time step dt=1.35 × 10^{-11} sec. Within 10000 iterations, the van der Waals bonds of the particles with a graphene

layer longer than 5 nm could not be broken. On the contrary, the van der Waals bonds of the layers whose length was smaller than 5 nm could be effectively broken.

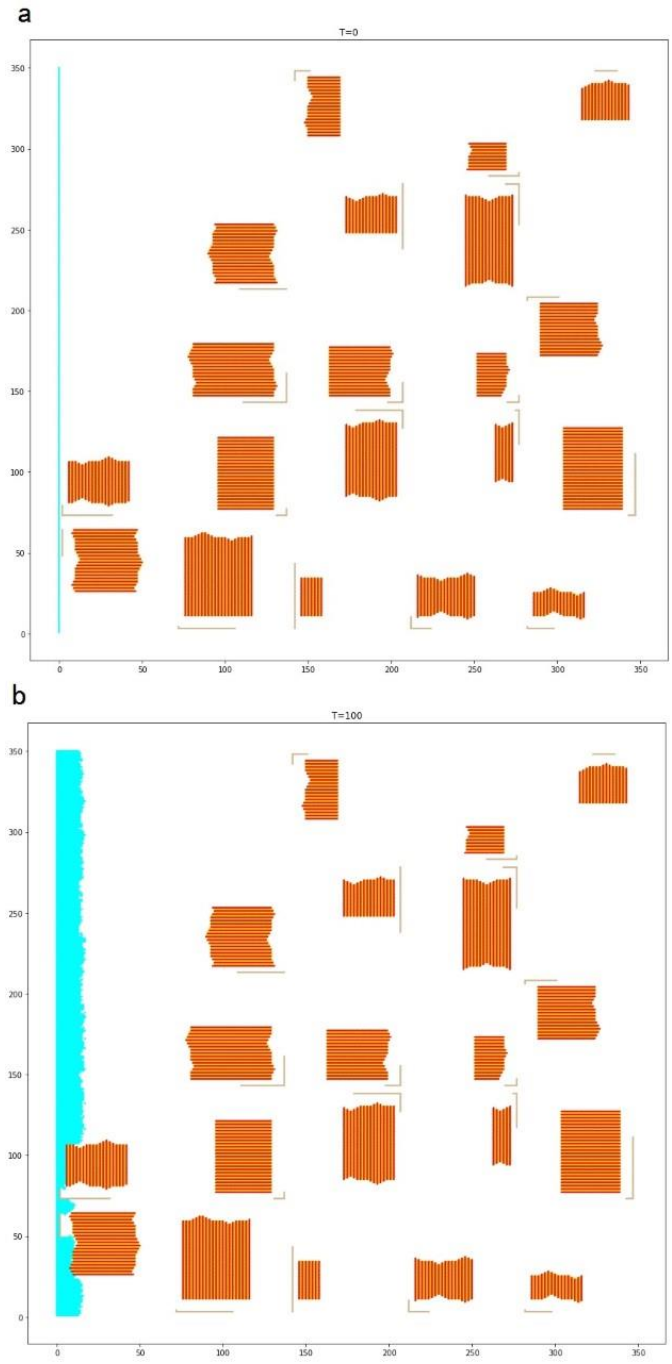

Figure 3.13 Snapshot of the coke particle diffusion process at iteration number (a) T=0, (b) T=100.

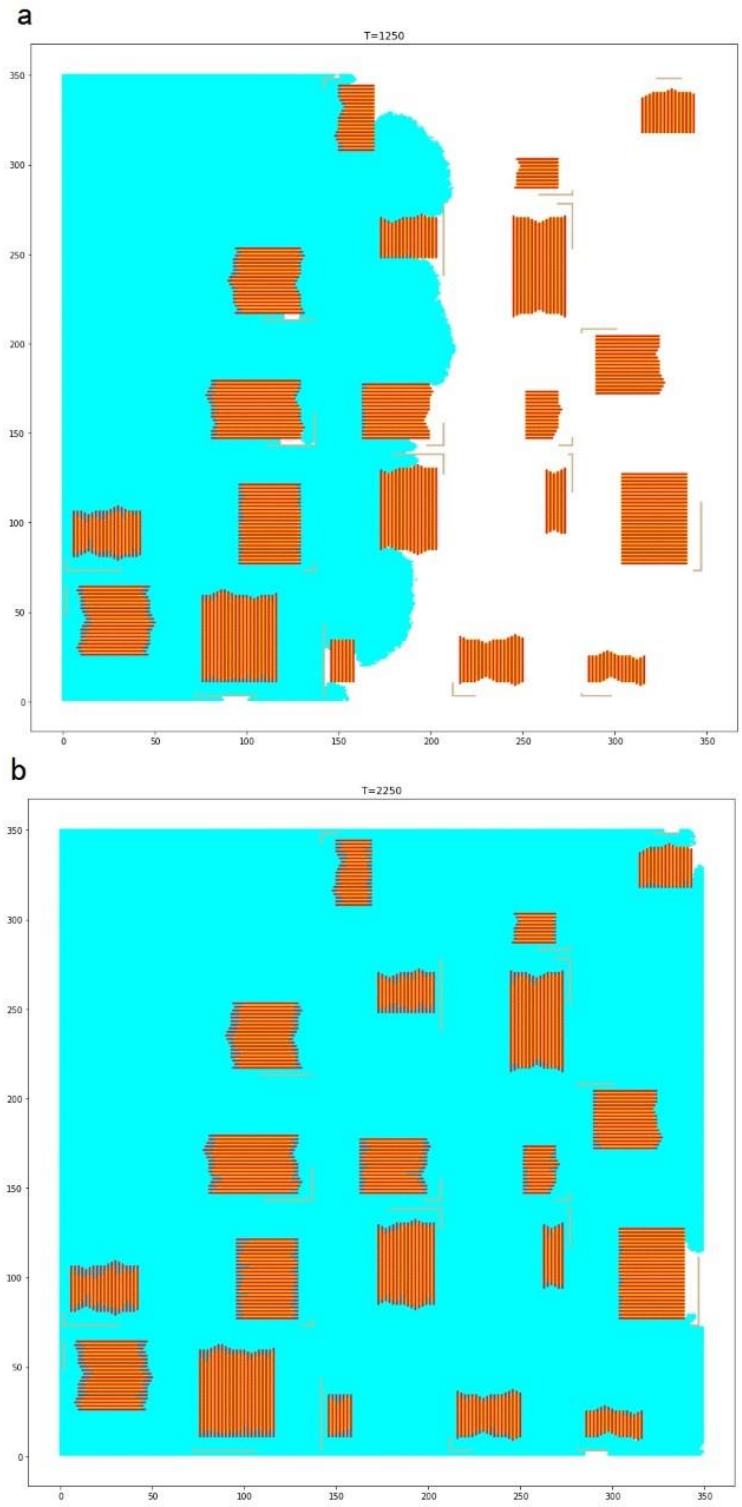

Figure 3.14 Snapshot of the coke particle diffusion process at iteration number (a) T=1250, (b) T=2250.

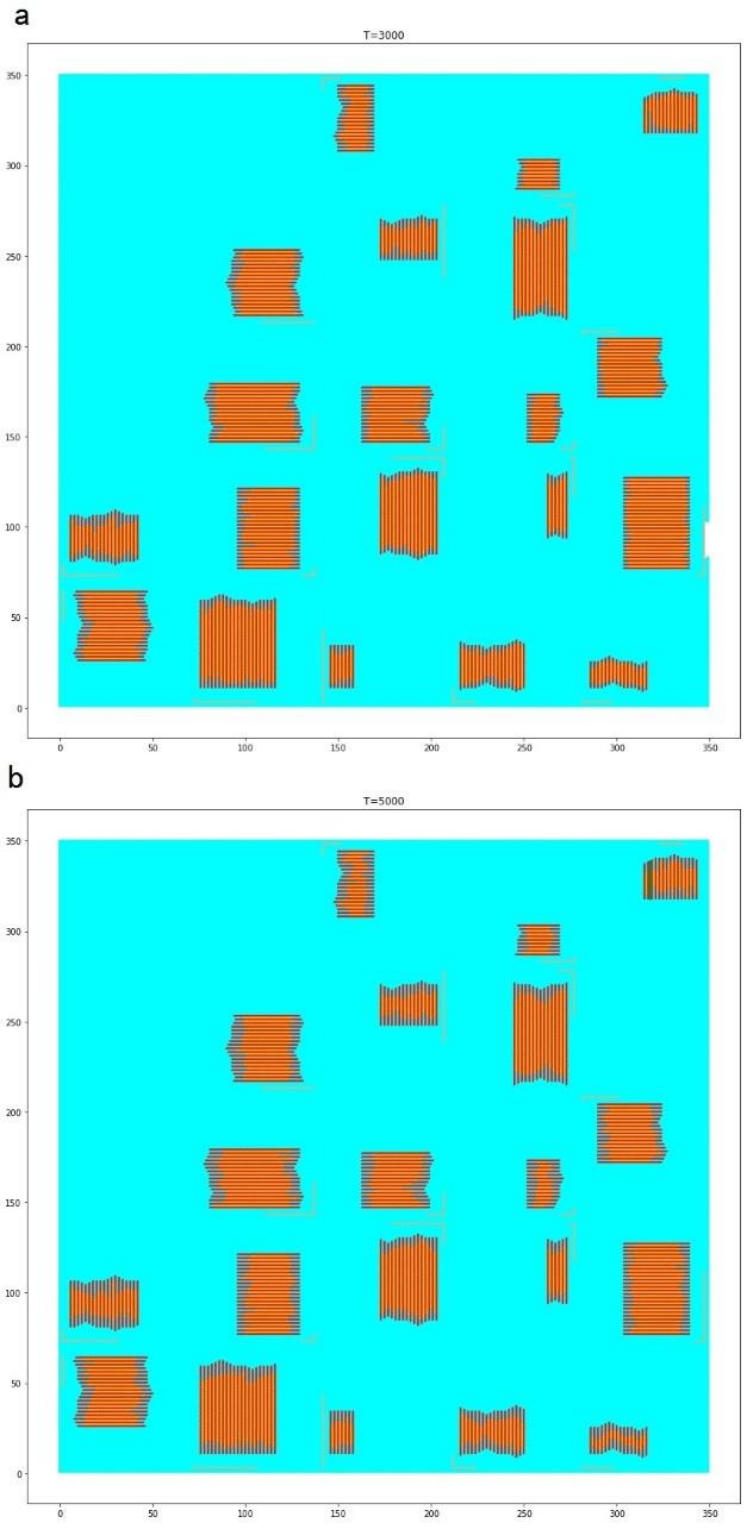

Figure 3.15 Snapshot of the coke particle diffusion process at iteration number (a) T=3000, (b) T=5000.

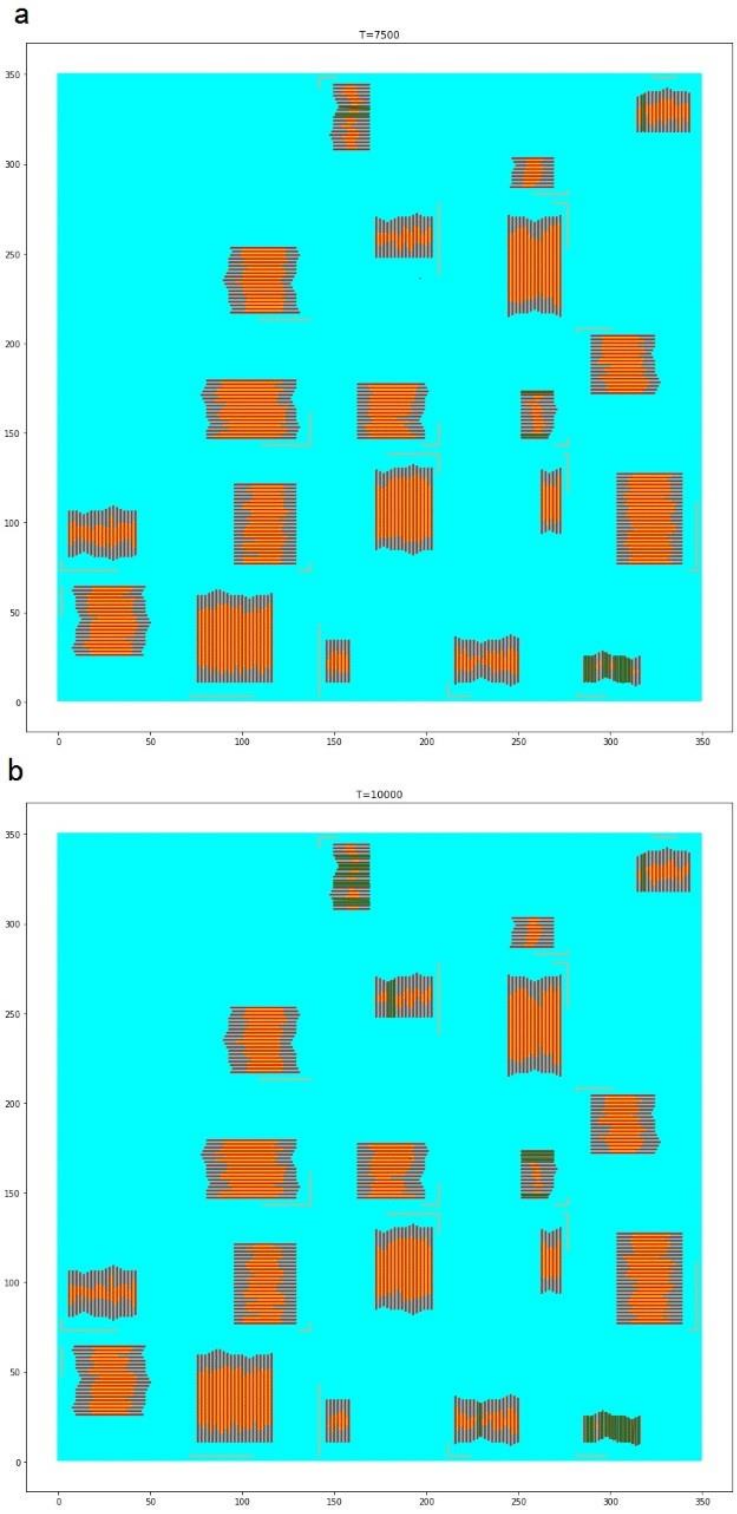

Figure 3.16 Snapshot of the coke particle diffusion process at iteration number (a) T=7500, (b) T=10000.

To quantitatively describe the process of acid diffusion over time of coke particles, the x coordinates are averaged using the P values via $<x^2>$, which is plotted against the time steps. When *s* = 0.44, a complete diffusion curve is obtained within 10000 iterations, as shown in **Figure 3.17**.

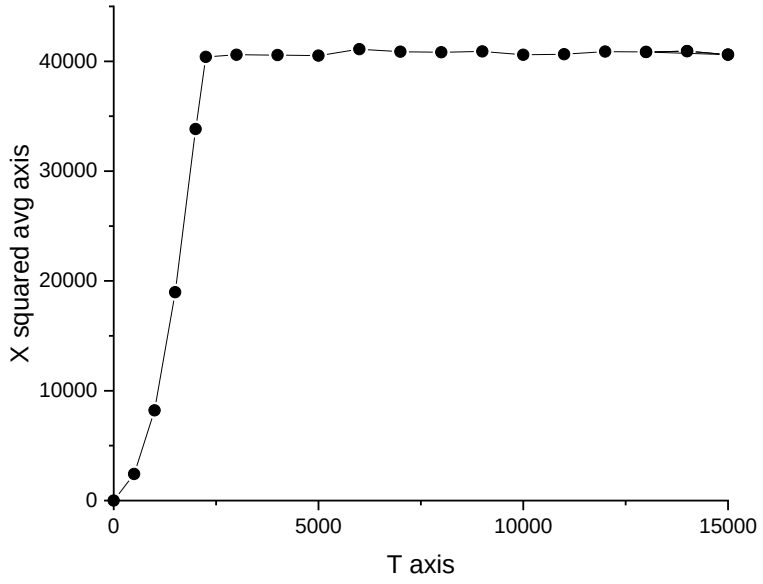

Figure 3.17 Diffusion curve $<x^2>$-t of coke particles when diffusivity variable *s* = 0.44.

For coke particles, diffusivity variable is *s*=0.44, it was found that the graphene layers began to peel off at the 5000th iteration, so made statistics on the size distribution of the acid diffusion process at the 0th, 5000th, 7500th and 10000th iteration, as shown in **Figure 3.19-3.22**. According to Ye et al. (Ye et al., 2013) result, coke graphene crystal structure size distribution is 5.8±1.7 nm, as shown in **Figure 3.18.** Therefore, at the 0th iteration, we made similar size distribution, which is 5.55±1.98 nm, as

shown in **Figure 3.19 (a)**. At the 5000th iteration, small graphene layers begin to peel off; the size distribution is 5.53±1.91 nm. At the 7500th iteration, more graphene layers were peeled off, forming an average size distribution in each size range, which does not conform to a Gaussian distribution. At the 10000th iteration, the size distribution peak is between 0-0.5 nm, and the size distribution is 0.8±0.31 nm. However, only a few small crystal structures were stripped. Therefore, we concluded through numerical simulations that within 10000 iterations, because of the large size of the coke carbon quantum dots, narrow size distribution cannot be obtained by breaking the van der Waals bonds using sulfuric acid diffusion.

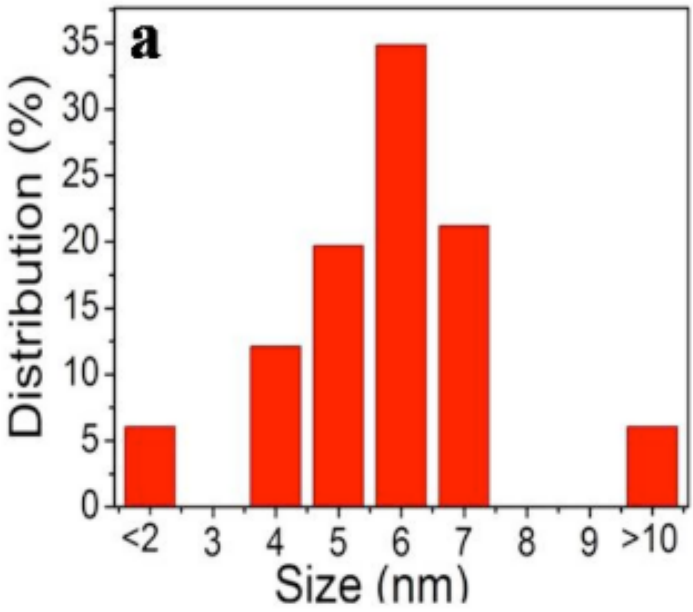

Figure 3.18 Coke carbon quantum dots size distribution according to Ye et al., size=5.8 ± 1.7 nm. Reprinted by permission from Springer Nature Nature Communications (Ye et al., 2013), copyright 2013.

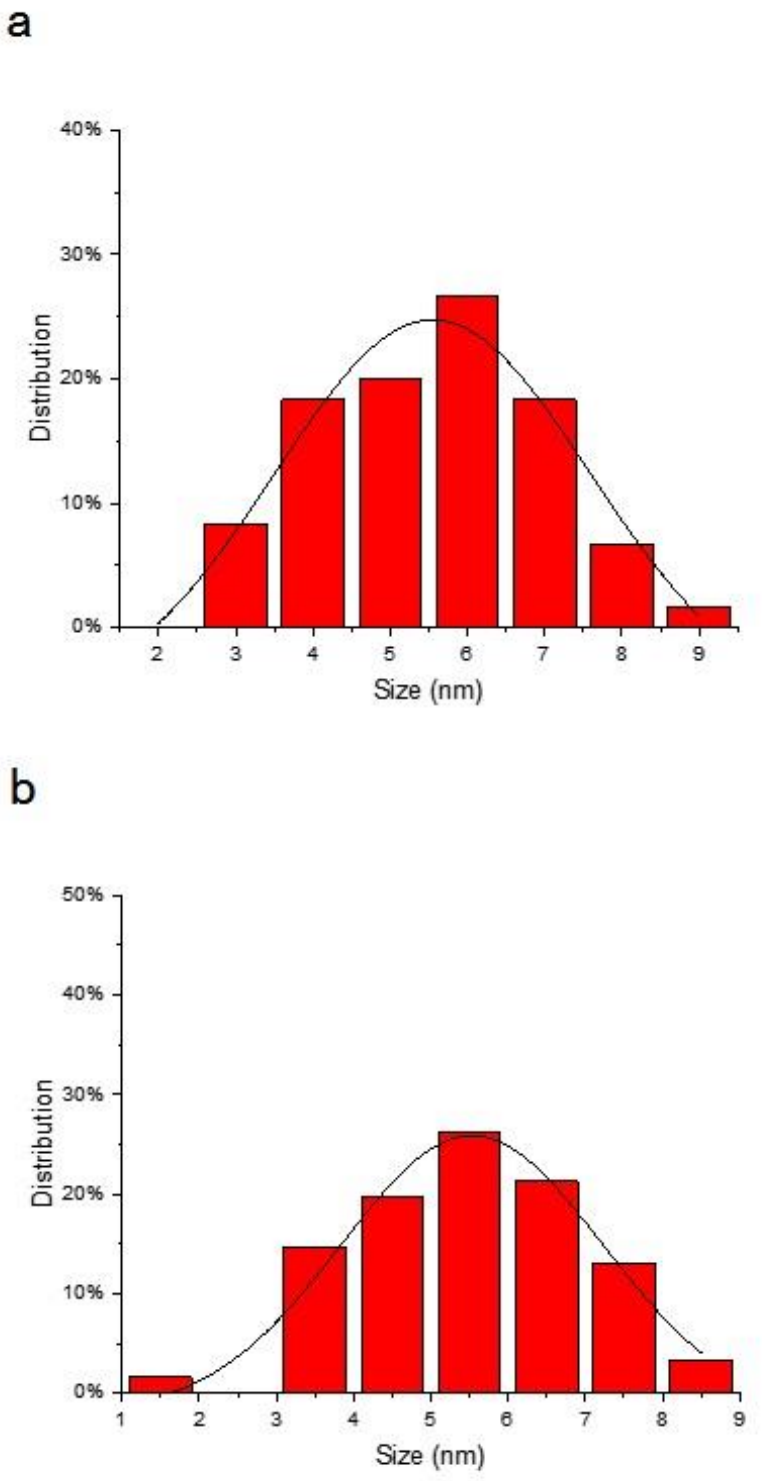

Figure 3.19 Coke carbon quantum dots size distribution at (a) T=0, size=5.55±1.98 nm; (b) T=5000, size=5.53±1.91 nm.

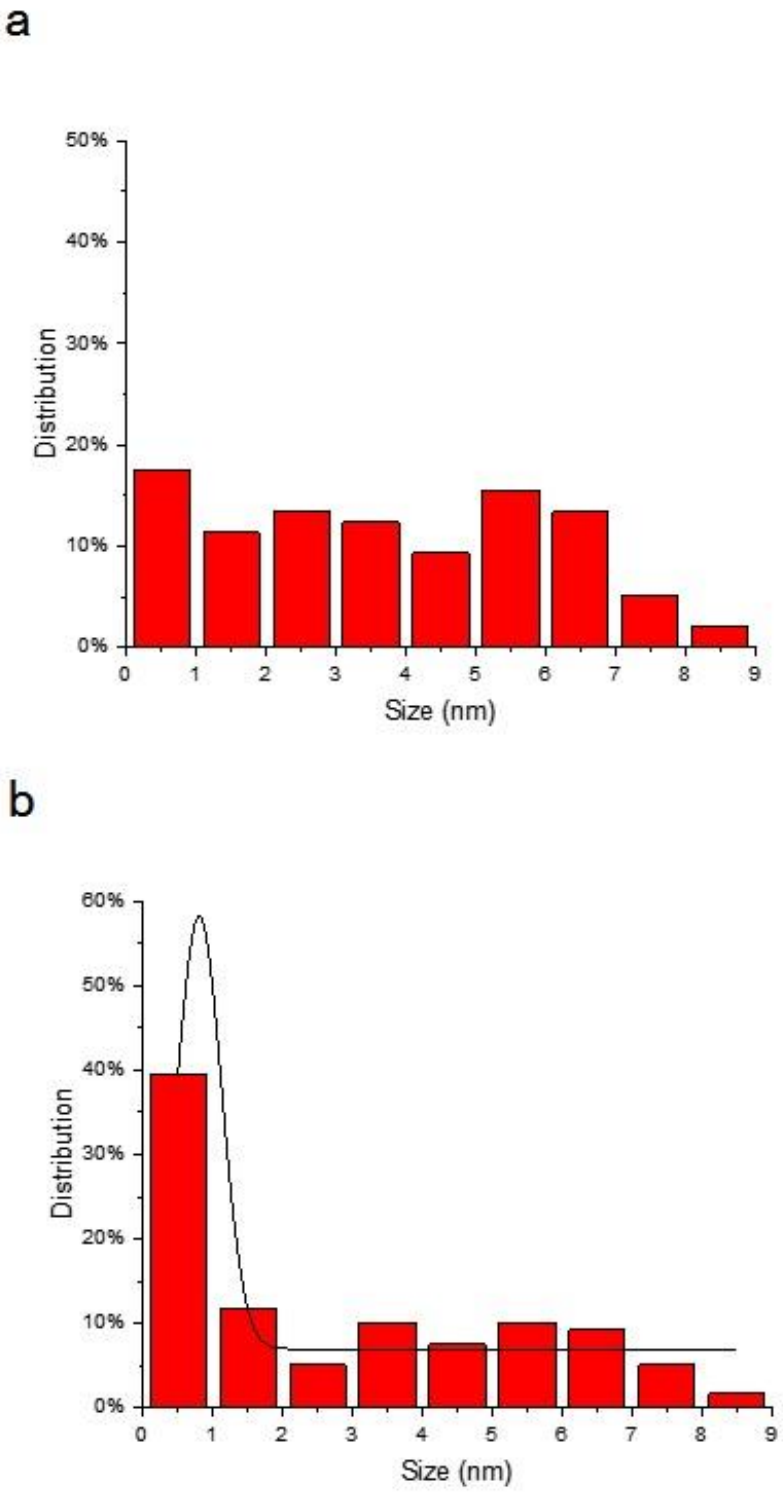

Figure 3.20 Coke carbon quantum dots size distribution at (a)T=7500; (b) T=10000, size=0.8±0.31 nm.

4 Conclusion

This study revealed the root cause of the broad size distribution in synthesizing carbon quantum dots from coal by sulfuric acid diffusion via numerical simulation. In particular, the results of this work attributed this issue to the breakage of the van der Waals bonds between the graphene layers by sulfuric acid diffusion. Whether the van der Waals bonds can be broken by acid diffusion depends on the size of the coal graphene structure. When graphene structure sizes are larger than 5 nm, because of the long diffusion time, the narrow size distribution cannot be obtained by breaking the van der Waals bonds. Due to the small average size of bituminous carbon quantum dots of 2.96 nm, a narrow size distribution can be obtained at the 1500th iteration, corresponding to the actual time of 34.2 h; however, coke carbon quantum dots average size is large of 5.8 nm, the van der Waals bonds cannot be broken, and narrow size distribution cannot be obtained by acid diffusion. The result uncovers the scientific basis of broad size distribution, guides the experimental approach to obtaining narrow size distributions, and avoid blind trials.

5 Reference

Ahirwar, S., Mallick, S., & Bahadur, D. (2017, Nov 30). Electrochemical Method To Prepare Graphene Quantum Dots and Graphene Oxide Quantum Dots. *ACS Omega*, *2*(11), 8343-8353. https://doi.org/10.1021/acsomega.7b01539

Arul, V., Edison, T. N., Lee, Y. R., & Sethuraman, M. G. (2017, Mar). Biological and catalytic applications of green synthesized fluorescent N-doped carbon dots using Hylocereus undatus. *J Photochem Photobiol B*, *168*, 142-148. https://doi.org/10.1016/j.jphotobiol.2017.02.007

Bawendi, M. G., Steigerwald, M. L., & Brus, L. E. (1990). The Quantum Mechanics of Larger Semiconductor Clusters ("Quantum Dots"). *Annual Review of Physical Chemistry*, *41*(1), 477-496. https://doi.org/10.1146/annurev.pc.41.100190.002401

Cai, T.-t., Liu, B., Pang, E.-n., Ren, W.-j., Li, S.-j., & Hu, S.-l. (2020). A review on the preparation and applications of coal-based fluorescent carbon dots. *New Carbon Materials*, *35*(6), 646-666. https://doi.org/10.1016/s1872-5805(20)60520-0

Calabro, R. L., Yang, D. S., & Kim, D. Y. (2018, Oct 1). Liquid-phase laser ablation synthesis of graphene quantum dots from carbon nano-onions: Comparison with chemical oxidation. *J Colloid Interface Sci, 527*, 132-140. https://doi.org/10.1016/j.jcis.2018.04.113

Chan, W. C., Maxwell, D. J., Gao, X., Bailey, R. E., Han, M., & Nie, S. (2002). Luminescent quantum dots for multiplexed biological detection and imaging. *Current opinion in biotechnology, 13(1)*, 40-46.

Chang, W., & Xu, G. (1993). Simulation of ionic diffusion in solid polymer electrolytes with correlated chain motion. *The Journal of chemical physics, 99*(3), 2001-2003. https://doi.org/10.1063/1.3600337

Chen, C. F., Park, C. H., Boudouris, B. W., Horng, J., Geng, B., Girit, C., Zettl, A., Crommie, M. F., Segalman, R. A., Louie, S. G., & Wang, F. (2011, Mar 31). Controlling inelastic light scattering quantum pathways in graphene. *Nature, 471*(7340), 617-620. https://doi.org/10.1038/nature09866

Deng, Y., Qian, J., & Zhou, Y. (2020). Solvothermal Synthesis and Inkjet Printing of Carbon Quantum Dots. *ChemistrySelect, 5*(47), 14930-14934. https://doi.org/10.1002/slct.202003487

Di, G., Zhu, Z., Dai, Q., Zhang, H., Shen, X., Qiu, Y., Huang, Y., Yu, J., Yin, D., & Küppers, S. (2020). Wavelength-dependent effects of carbon quantum dots on the photocatalytic activity of g-C3N4 enabled by LEDs. *Chemical Engineering Journal, 379*. https://doi.org/10.1016/j.cej.2019.122296

Ding, H., Wei, J. S., Zhang, P., Zhou, Z. Y., Gao, Q. Y., & Xiong, H. M. (2018, May). Solvent-Controlled Synthesis of Highly Luminescent Carbon Dots with a Wide Color Gamut and Narrowed Emission Peak Widths. *Small, 14*(22), e1800612. https://doi.org/10.1002/smll.201800612

Donega´, C. d. M. (2011, Mar). Synthesis and properties of colloidal heteronanocrystals. *Chem Soc Rev, 40*(3), 1512-1546. https://doi.org/10.1039/c0cs00055h

Dong, Y., Chen, C., Zheng, X., Gao, L., Cui, Z., Yang, H., Guo, C., Chi, Y., & Li, C. M. (2012). One-step and high yield simultaneous preparation of single- and multi-layer graphene quantum dots from CX-72 carbon black. *Journal of Materials Chemistry, 22*(18). https://doi.org/10.1039/c2jm30658a

Dong, Y., Pang, H., Yang, H. B., Guo, C., Shao, J., Chi, Y., Li, C. M., & Yu, T. (2013,

Jul 22). Carbon-based dots co-doped with nitrogen and sulfur for high quantum yield and excitation-independent emission. *Angew Chem Int Ed Engl*, *52*(30), 7800-7804. https://doi.org/10.1002/anie.201301114

Gul, U., Kanwal, S., Tabassum, S., Gilani, M. A., & Rahim, A. (2020, Jan 16). Microwave-assisted synthesis of carbon dots as reductant and stabilizer for silver nanoparticles with enhanced-peroxidase like activity for colorimetric determination of hydrogen peroxide and glucose. *Mikrochim Acta*, *187*(2), 135. https://doi.org/10.1007/s00604-019-4098-x

Guo, Z., Wang, Q., Shen, T., Hou, X., Kuang, J., Liu, W., & Cao, W. (2019). Synthesis of 3D CQDs/urchin-like and yolk-shell TiO2 hierarchical structure with enhanced photocatalytic properties. *Ceramics International*, *45*(5), 5858-5865. https://doi.org/10.1016/j.ceramint.2018.12.052

Harris, C. S., Nitzan, A., Ratner, M. A., & Shriver, D. F. . (1986). Particle motion through a dynamically disordered medium: The effects of bond correlation and application to polymer solid electrolytes. *Solid state ionics*, *18*, 151-155.

Hsu, P.-C., Shih, Z.-Y., Lee, C.-H., & Chang, H.-T. (2012). Synthesis and analytical applications of photoluminescent carbon nanodots. *Green Chemistry*, *14*(4).

https://doi.org/10.1039/c2gc16451e

Huang, C., Dong, H., Su, Y., Wu, Y., Narron, R., & Yong, Q. (2019, Mar 7). Synthesis of Carbon Quantum Dot Nanoparticles Derived from Byproducts in Bio-Refinery Process for Cell Imaging and In Vivo Bioimaging. *Nanomaterials (Basel), 9*(3). https://doi.org/10.3390/nano9030387

Huang, J., Li, L., Chen, J., Ma, F., & Yu, Y. (2020). Broad spectrum response flower spherical-like composites CQDs@CdIn2S4/CdS modified by CQDs with up-conversion property for photocatalytic degradation and water splitting. *International Journal of Hydrogen Energy, 45*(3), 1822-1836. https://doi.org/10.1016/j.ijhydene.2019.11.078

Jiang, Z., Sun, H., Wang, T., Wang, B., Wei, W., Li, H., Yuan, S., An, T., Zhao, H., Yu, J., & Wong, P. K. (2018). Nature-based catalyst for visible-light-driven photocatalytic CO2 reduction. *Energy & Environmental Science, 11*(9), 2382-2389. https://doi.org/10.1039/c8ee01781f

Kim, S., Hwang, S. W., Kim, M. K., Shin, D. Y., Shin, D. H., Kim, C. O., ... & Hong, B. H. . (2012). Anomalous behaviors of visible luminescence from graphene quantum dots: interplay between size and shape. *ACS Nano, 6*(9), 8203-8208.

Kumar, V., Singh, V., Umrao, S., Parashar, V., Abraham, S., Singh, A. K., Nath, G., Saxena, P. S., & Srivastava, A. (2014). Facile, rapid and upscaled synthesis of green luminescent functional graphene quantum dots for bioimaging. *RSC Advances, 4*(40). https://doi.org/10.1039/c4ra01735h

Kwon, W., Kim, Y. H., Lee, C. L., Lee, M., Choi, H. C., Lee, T. W., & Rhee, S. W. (2014, Mar 12). Electroluminescence from graphene quantum dots prepared by amidative cutting of tattered graphite. *Nano Lett, 14*(3), 1306-1311. https://doi.org/10.1021/nl404281h

Leshin, V. S., Sorokina, N. E., & Avdeev, V. V. . (2004). Electrochemical synthesis and thermal properties of graphite bisulfate. *Inorganic materials, 40*(6), 649-655.

Li, H., He, X., Kang, Z., Huang, H., Liu, Y., Liu, J., Lian, S., Tsang, C. H., Yang, X., & Lee, S. T. (2010, Jun 14). Water-soluble fluorescent carbon quantum dots and photocatalyst design. *Angew Chem Int Ed Engl, 49*(26), 4430-4434. https://doi.org/10.1002/anie.200906154

Li, L.-s., & Yan, X. (2010). Colloidal Graphene Quantum Dots. *The Journal of Physical Chemistry Letters, 1*(17), 2572-2576.

https://doi.org/10.1021/jz100862f

Li, Q., Ohulchanskyy, T. Y., Liu, R., Koynov, K., Wu, D., Best, A., ... & Prasad, P. N. (2010). Photoluminescent carbon dots as biocompatible nanoprobes for targeting cancer cells in vitro. The Journal of Physical Chemistry C, 114(28), 12062-12068. (2010). Photoluminescent carbon dots as biocompatible nanoprobes for targeting cancer cells in vitro. *The Journal of Physical Chemistry C, 114*(28), 12062-12068.

Li, Y., Hu, Y., Zhao, Y., Shi, G., Deng, L., Hou, Y., & Qu, L. (2011, Feb 8). An electrochemical avenue to green-luminescent graphene quantum dots as potential electron-acceptors for photovoltaics. *Adv Mater, 23*(6), 776-780. https://doi.org/10.1002/adma.201003819

Li, Y., Li, W., Yang, X., Kang, Y., Zhang, H., Liu, Y., & Lei, B. (2020). Salvia Miltiorrhiza-Derived Carbon Dots as Scavengers of Reactive Oxygen Species for Reducing Oxidative Damage of Plants. *ACS Applied Nano Materials, 4*(1), 113-120. https://doi.org/10.1021/acsanm.0c02419

Liu, M. L., Chen, B. B., Li, C. M., & Huang, C. Z. (2019). Carbon dots: synthesis, formation mechanism, fluorescence origin and sensing applications. *Green*

Chemistry, 21(3), 449-471. https://doi.org/10.1039/c8gc02736f

Liu, R., Wu, D., Liu, S., Koynov, K., Knoll, W., & Li, Q. (2009). An aqueous route to multicolor photoluminescent carbon dots using silica spheres as carriers. *Angew Chem Int Ed Engl, 48*(25), 4598-4601. https://doi.org/10.1002/anie.200900652

Liu, W., Li, M., Jiang, G., Li, G., Zhu, J., Xiao, M., Zhu, Y., Gao, R., Yu, A., Feng, M., & Chen, Z. (2020). Graphene Quantum Dots-Based Advanced Electrode Materials: Design, Synthesis and Their Applications in Electrochemical Energy Storage and Electrocatalysis. *Advanced Energy Materials, 10*(29). https://doi.org/10.1002/aenm.202001275

Liu, Y., Huang, H., Cao, W., Mao, B., Liu, Y., & Kang, Z. (2020). Advances in carbon dots: from the perspective of traditional quantum dots. *Materials Chemistry Frontiers, 4*(6), 1586-1613. https://doi.org/10.1039/d0qm00090f

Loukanov, A., Sekiya, R., Yoshikawa, M., Kobayashi, N., Moriyasu, Y., & Nakabayashi, S. (2016). Photosensitizer-Conjugated Ultrasmall Carbon Nanodots as Multifunctional Fluorescent Probes for Bioimaging. *The Journal of Physical Chemistry C, 120*(29), 15867-15874.

https://doi.org/10.1021/acs.jpcc.5b11721

Manikandan, V., & Lee, N. Y. (2022, Sep). Green synthesis of carbon quantum dots and their environmental applications. *Environ Res, 212*(Pt B), 113283. https://doi.org/10.1016/j.envres.2022.113283

Molaei, M. J. (2020). Principles, mechanisms, and application of carbon quantum dots in sensors: a review. *Analytical Methods, 12*(10), 1266-1287. https://doi.org/10.1039/c9ay02696g

Mueller, M. L., Yan, X., Dragnea, B., & Li, L. S. (2011, Jan 12). Slow hot-carrier relaxation in colloidal graphene quantum dots. *Nano Lett, 11*(1), 56-60. https://doi.org/10.1021/nl102712x

Nair, A., Haponiuk, J. T., Thomas, S., & Gopi, S. (2020, Dec). Natural carbon-based quantum dots and their applications in drug delivery: A review. *Biomed Pharmacother, 132*, 110834. https://doi.org/10.1016/j.biopha.2020.110834

Nekoueian, K., Amiri, M., Sillanpaa, M., Marken, F., Boukherroub, R., & Szunerits, S. (2019, Jul 29). Carbon-based quantum particles: an electroanalytical and biomedical perspective. *Chem Soc Rev, 48*(15), 4281-4316.

https://doi.org/10.1039/c8cs00445e

Newman Monday, Y., Abdullah, J., Yusof, N. A., Abdul Rashid, S., & Shueb, R. H. (2021). Facile Hydrothermal and Solvothermal Synthesis and Characterization of Nitrogen-Doped Carbon Dots from Palm Kernel Shell Precursor. *Applied Sciences, 11*(4). https://doi.org/10.3390/app11041630

Nilewski, L., Mendoza, K., Jalilov, A. S., Berka, V., Wu, G., Sikkema, W. K. A., Metzger, A., Ye, R., Zhang, R., Luong, D. X., Wang, T., McHugh, E., Derry, P. J., Samuel, E. L., Kent, T. A., Tsai, A. L., & Tour, J. M. (2019, May 8). Highly Oxidized Graphene Quantum Dots from Coal as Efficient Antioxidants. *ACS Appl Mater Interfaces, 11*(18), 16815-16821. https://doi.org/10.1021/acsami.9b01082

Pan, D., Zhang, J., Li, Z., & Wu, M. (2010, Feb 9). Hydrothermal route for cutting graphene sheets into blue-luminescent graphene quantum dots. *Adv Mater, 22*(6), 734-738. https://doi.org/10.1002/adma.200902825

Pang, C., & Gong, Y. (2019, Jul 10). Current Status and Future Prospects of Semiconductor Quantum Dots in Botany. *J Agric Food Chem, 67*(27), 7561-7568. https://doi.org/10.1021/acs.jafc.9b00730

Pei, S., Wei, Q., Huang, K., Cheng, H. M., & Ren, W. (2018, Jan 10). Green synthesis of graphene oxide by seconds timescale water electrolytic oxidation. *Nat Commun, 9*(1), 145. https://doi.org/10.1038/s41467-017-02479-z

Peng, J., Gao, W., Gupta, B. K., Liu, Z., Romero-Aburto, R., Ge, L., Song, L., Alemany, L. B., Zhan, X., Gao, G., Vithayathil, S. A., Kaipparettu, B. A., Marti, A. A., Hayashi, T., Zhu, J. J., & Ajayan, P. M. (2012, Feb 8). Graphene quantum dots derived from carbon fibers. *Nano Lett, 12*(2), 844-849. https://doi.org/10.1021/nl2038979

Qiao, Z. A., Wang, Y., Gao, Y., Li, H., Dai, T., Liu, Y., & Huo, Q. (2010, Dec 14). Commercially activated carbon as the source for producing multicolor photoluminescent carbon dots by chemical oxidation. *Chem Commun (Camb), 46*(46), 8812-8814. https://doi.org/10.1039/c0cc02724c

Raj, A. M., & Balachandran, M. (2020). Coal-Based Fluorescent Zero-Dimensional Carbon Nanomaterials: A Short Review. *Energy & Fuels, 34*(11), 13291-13306. https://doi.org/10.1021/acs.energyfuels.0c02619

Ran, Y., Wang, S., Yin, Q., Wen, A., Peng, X., Long, Y., & Chen, S. (2020, Sep).

Green synthesis of fluorescent carbon dots using chloroplast dispersions as precursors and application for Fe(3+) ion sensing. *Luminescence, 35*(6), 870-876. https://doi.org/10.1002/bio.3794

Ray, S. C., Saha, A., Jana, N. R., & Sarkar, R. (2009). Fluorescent carbon nanoparticles: synthesis, characterization, and bioimaging application. . *The Journal of Physical Chemistry C, 113*(43), 18546-18551.

Saikia, M., Hower, J. C., Das, T., Dutta, T., & Saikia, B. K. (2019). Feasibility study of preparation of carbon quantum dots from Pennsylvania anthracite and Kentucky bituminous coals. *Fuel, 243*, 433-440. https://doi.org/10.1016/j.fuel.2019.01.151

Shaari, N., Kamarudin, S. K., & Bahru, R. (2020). Carbon and graphene quantum dots in fuel cell application: An overview. *International Journal of Energy Research*. https://doi.org/10.1002/er.5889

Sk, M. A., Ananthanarayanan, A., Huang, L., Lim, K. H., & Chen, P. (2014). Revealing the tunable photoluminescence properties of graphene quantum dots. *J. Mater. Chem. C, 2*(34), 6954-6960. https://doi.org/10.1039/c4tc01191k

Son, C. Y., & Wang, Z. G. (2020, Sep 14). Ion transport in small-molecule and polymer electrolytes. *J Chem Phys, 153*(10), 100903. https://doi.org/10.1063/5.0016163

Song, Y., Zhu, S., Zhang, S., Fu, Y., Wang, L., Zhao, X., & Yang, B. (2015). Investigation from chemical structure to photoluminescent mechanism: a type of carbon dots from the pyrolysis of citric acid and an amine. *Journal of Materials Chemistry C, 3*(23), 5976-5984. https://doi.org/10.1039/c5tc00813a

Sun, Y. P., Zhou, B., Lin, Y., Wang, W., Fernando, K. S., Pathak, P., ... & Xie, S. Y. . (2006). Quantum-sized carbon dots for bright and colorful photoluminescence. *Journal of the American Chemical Society, 128*(24), 7756-7757.

Wang, D., Liu, L., Wang, Y., Fan, C., & Huang, W. (2020). A new insight on the role of CQDs in driving BiOBr into broader-spectrum-response: Dual function of up-conversion and photosensitization effect. *Chemical Physics Letters, 747*. https://doi.org/10.1016/j.cplett.2020.137340

Wu, J., Lu, Y., Feng, S., Wu, Z., Lin, S., Hao, Z., Yao, T., Li, X., Zhu, H., & Lin, S. (2018). The Interaction between Quantum Dots and Graphene: The Applications in Graphene-Based Solar Cells and Photodetectors. *Advanced*

Functional Materials, 28(50). https://doi.org/10.1002/adfm.201804712

Wu, X., Tian, F., Wang, W., Chen, J., Wu, M., & Zhao, J. X. (2013, Aug 21). Fabrication of highly fluorescent graphene quantum dots using L-glutamic acid for in vitro/in vivo imaging and sensing. *J Mater Chem C Mater, 1*(31), 4676-4684. https://doi.org/10.1039/C3TC30820K

Xu, A., Wang, G., Li, Y., Dong, H., Yang, S., He, P., & Ding, G. (2020, Nov 3). Carbon-Based Quantum Dots with Solid-State Photoluminescent: Mechanism, Implementation, and Application. *Small*, e2004621. https://doi.org/10.1002/smll.202004621

Xu, G. (1992). The effects of chain segment motion on ionic diffusion in solid polymer electrolytes. *Solid state ionics*, *50*(3-4), 345-347.

Xu, K. J., Wang, R. T., Xu, A. F., Chen, J. Y., & Xu, G. (2020, Oct 28). Hysteresis and Instability Predicted in Moisture Degradation of Perovskite Solar Cells. *ACS Appl Mater Interfaces, 12*(43), 48882-48889. https://doi.org/10.1021/acsami.0c17323

Xu, Q., Kuang, T., Liu, Y., Cai, L., Peng, X., Sreenivasan Sreeprasad, T., Zhao, P., Yu,

Z., & Li, N. (2016, Dec 7). Heteroatom-doped carbon dots: synthesis, characterization, properties, photoluminescence mechanism and biological applications. *J Mater Chem B, 4*(45), 7204-7219. https://doi.org/10.1039/c6tb02131j

Xu X, R. R., Gu Y, et al. (2004). Electrophoretic analysis and purification of fluorescent single-walled carbon nanotube fragments.

Xu, Y., Wu, M., Liu, Y., Feng, X. Z., Yin, X. B., He, X. W., & Zhang, Y. K. (2013, Feb 11). Nitrogen-doped carbon dots: a facile and general preparation method, photoluminescence investigation, and imaging applications. *Chemistry, 19*(7), 2276-2283. https://doi.org/10.1002/chem.201203641

Yan, F., Wang, Y., Zang, Y., Sun, J., Yi, C., Xu, M., & Xu, J. (2021). Introduction to the Performance and Mechanism of Various Photocatalytic Materials Compounded with Carbon Dots. *Particle & Particle Systems Characterization, 38*(9). https://doi.org/10.1002/ppsc.202100082

Yan, Y., Gong, J., Chen, J., Zeng, Z., Huang, W., Pu, K., Liu, J., & Chen, P. (2019, May). Recent Advances on Graphene Quantum Dots: From Chemistry and Physics to Applications. *Adv Mater, 31*(21), e1808283.

https://doi.org/10.1002/adma.201808283

Ye, R., Peng, Z., Metzger, A., Lin, J., Mann, J. A., Huang, K., Xiang, C., Fan, X., Samuel, E. L., Alemany, L. B., Marti, A. A., & Tour, J. M. (2015, Apr 1). Bandgap engineering of coal-derived graphene quantum dots. *ACS Appl Mater Interfaces, 7*(12), 7041-7048. https://doi.org/10.1021/acsami.5b01419

Ye, R., Xiang, C., Lin, J., Peng, Z., Huang, K., Yan, Z., Cook, N. P., Samuel, E. L., Hwang, C. C., Ruan, G., Ceriotti, G., Raji, A. R., Marti, A. A., & Tour, J. M. (2013). Coal as an abundant source of graphene quantum dots. *Nat Commun, 4*, 2943. https://doi.org/10.1038/ncomms3943

Yeh, T. F., Huang, W. L., Chung, C. J., Chiang, I. T., Chen, L. C., Chang, H. Y., Su, W. C., Cheng, C., Chen, S. J., & Teng, H. (2016, Jun 2). Elucidating Quantum Confinement in Graphene Oxide Dots Based On Excitation-Wavelength-Independent Photoluminescence. *J Phys Chem Lett, 7*(11), 2087-2092. https://doi.org/10.1021/acs.jpclett.6b00752

Younis, M. R., He, G., Lin, J., & Huang, P. (2020). Recent Advances on Graphene Quantum Dots for Bioimaging Applications. *Front Chem, 8*, 424. https://doi.org/10.3389/fchem.2020.00424

Yuan, F., Li, S., Fan, Z., Meng, X., Fan, L., & Yang, S. (2016). Shining carbon dots: Synthesis and biomedical and optoelectronic applications. *Nano Today, 11*(5), 565-586.

Zhang, J., & Yu, S.-H. (2016). Carbon dots: large-scale synthesis, sensing and bioimaging. *Materials Today, 19*(7), 382-393. https://doi.org/10.1016/j.mattod.2015.11.008

Zhang, X., Wang, S., Zhu, C., Liu, M., Ji, Y., Feng, L., Tao, L., & Wei, Y. (2013, May 1). Carbon-dots derived from nanodiamond: photoluminescence tunable nanoparticles for cell imaging. *J Colloid Interface Sci, 397*, 39-44. https://doi.org/10.1016/j.jcis.2013.01.063

Zhang, Y., Li, K., Ren, S., Dang, Y., Liu, G., Zhang, R., Zhang, K., Long, X., & Jia, K. (2019). Coal-Derived Graphene Quantum Dots Produced by Ultrasonic Physical Tailoring and Their Capacity for Cu(II) Detection. *ACS Sustainable Chemistry & Engineering, 7*(11), 9793-9799. https://doi.org/10.1021/acssuschemeng.8b06792

Zhang, Z., Zhang, J., Chen, N., & Qu, L. (2012). Graphene quantum dots: an

emerging material for energy-related applications and beyond. *Energy & Environmental Science, 5*(10). https://doi.org/10.1039/c2ee22982j

Zheng, X. T., Ananthanarayanan, A., Luo, K. Q., & Chen, P. (2015, Apr 8). Glowing graphene quantum dots and carbon dots: properties, syntheses, and biological applications. *Small, 11*(14), 1620-1636. https://doi.org/10.1002/smll.201402648

Zhu, S., Song, Y., Zhao, X., Shao, J., Zhang, J., & Yang, B. (2015). The photoluminescence mechanism in carbon dots (graphene quantum dots, carbon nanodots, and polymer dots): current state and future perspective. *Nano Research, 8*(2), 355-381. https://doi.org/10.1007/s12274-014-0644-3

6 Appendix

Program of bituminous, modified from Kevin Xu (K. J. Xu et al., 2020).

```
import sys

import numpy as np

import random

import matplotlib.pyplot as plt

import time

from matplotlib.colors import ListedColormap, LinearSegmentedColormap

#initialization matrix，G is color

m = 200

n = 200

Hlite = 40

Wlite = 40

startP = 0

P = np.full((m,n), 0.0)

W = np.full((m,n,4), random.uniform(0, 99)/100)

G = np.full((m,n), 0)

# small geometry

def create_graph():

    cos = [-3,-2,-1,0,1,2,3,2,1,0,-1,-2,-3,-2,-1,0,1,2,3,2,1,0,-1,-2,-3,-2,-1,0,1,2,3,2,1,0,-1,-2,-3,-2,-1,0,1,2,3,2,1,0,-1,-2,-3,-2,-1,0,1,2,3,2,1,0,-1,-2,-3,-2,-1,0,1,2,3,2,1,0,-1,-2,-3,-2,-1,0,1,2,3,2,1,0,-1,-2,-3,-
```

```
2,-1,0,1,2,3,2,1,0,-1,-2,-3]
    sin = [3,2,1,0,-1,-2,-3,-2,-1,0,1,2,3,2,1,0,-1,-2,-3,-2,-1,0,1,2,3,2,1,0,-1,-2,-3,-2,-
1,0,1,2,3,2,1,0,-1,-2,-3,-2,-1,0,1,2,3,2,1,0,-1,-2,-3,-2,-1,0,1,2,3,2,1,0,-1,-2,-3,-2,-
1,0,1,2,3,2,1,0,-1,-2,-3,-2,-1,0,1,2,3]
    nothing =
[0,0,0,0,0,0,0,0,0,0,0,0,0,0,0,0,0,0,0,0,0,0,0,0,0,0,0,0,0,0,0,0,0,0,0,0,0,0,0,0,0,0,0,0,0,0
,0,0,0,0,0,0,0,0,0,0,0,0,0,0,0,0,0,0,0,0,0,0,0,0,0,0,0,0,0,0,0,0,0,0,0,0,0,0,0,0,0,0,0,0,0,0
,0,0,0,0,0,0,0,0,0,0,0,0,0,0,0,0,0,0,0,0,0,0,0,0,0,0,0,0,0,0,0,0,0,0,0,0,0,0,0,0,0]
    baseA=random.gauss(17,6)
    baseC=random.gauss(9,3)
    baseH = round(baseA)
    baseW = round(baseC)
    Glite = np.full((Hlite,Wlite), 0)
    startnum = random.randint(0, 30)
    edge1 = random.choice([cos,sin,nothing])[startnum:startnum+baseW]
    edge2 = random.choice([cos,sin,nothing])[startnum:startnum+baseW]
    for i  in range(baseW-1):
        #red
        redC = baseH + edge1[i] + edge2[i]
        redCN =0
        if i + 1 <= baseW:
```

```
    redCN = baseH + edge1[i+1] + edge2[i+1]
for j in  range(0,baseH-1):
    Glite[i*2+4][j+5] = 1
    if i< baseW-2:
        Glite[i*2+4+1][j+5] = 2
if edge1[i] != 0:
    for k in range(0,abs(edge1[i])-1):
        if edge1[i] >0 :
            Glite[i*2+4][5+baseH+k-1] = 1
        elif edge1[i] < 0 :
            Glite[i*2+4][5+baseH-k-1] = 0
if edge2[i] !=0:
    for l in range(0,abs(edge2[i])-1):
        if edge2[i] >0 :
            Glite[i*2+4][5-l] = 1
        elif edge2[i] < 0 :
            Glite[i*2+4][5+l] = 0
#yellow
if i < baseW -2:
    if redCN >= redC:
        if edge1[i] != 0:
```

```
            for k in range(0,abs(edge1[i])-1):
                if edge1[i] >0 :
                    Glite[i*2+4+1][5+baseH+k-1] = 2
                elif edge1[i] < 0 :
                    Glite[i*2+4+1][5+baseH-k-1] = 0
        if edge2[i] !=0:
            for l in range(0,abs(edge2[i])-1):
                if edge2[i] >0 :
                    Glite[i*2+4+1][5-l] = 2
                elif edge2[i] < 0 :
                    Glite[i*2+4+1][5+l] = 0
    else:
        if edge1[i+1] != 0:
            for k in range(0,abs(edge1[i+1])-1):
                if edge1[i+1] >0 :
                    Glite[i*2+4+1][5+baseH+k-1] = 2
                elif edge1[i] < 0 :
                    Glite[i*2+4+1][5+baseH-k-1] = 0
        if edge2[i+1] !=0:
            for l in range(0,abs(edge2[i+1])-1):
                if edge2[i+1] >0 :
```

```
                    Glite[i*2+4+1][5-l] = 2
                elif edge2[i+1] < 0 :
                    Glite[i*2+4+1][5+l] = 0
        #brown
        brownNum = random.randint(11, 28)
        brownStart = random.randint(0,baseW)
    for b in range(0,brownNum):
        if brownStart*2 - b -1>=0:
            Glite[brownStart*2 - b][1] = 3
        else:
            Glite[1][1+brownNum-b] = 3
    for z in range(0,random.randint(0, 3)):
        Glite = np.rot90(Glite)
    return Glite
# small geometry random position
def create_big():
    RESULT_HEIGHT = m
    RESULT_WIDTH = n
    ROW_COUNT = 5
    COL_COUNT = 5
    GRAPH_COUNT = 21
```

```
    data = np.zeros((RESULT_HEIGHT, RESULT_WIDTH), dtype=int)
    ids =
random.sample([1,2,3,4,5,6,7,8,9,10,11,12,13,14,15,16,17,18,19,20,21,22,23,24],GRA
PH_COUNT)
    for i in range(0,GRAPH_COUNT-1):
        g = create_graph()
        gr, gc = g.shape
        brindex = ids[i] // ROW_COUNT
        bcindex = ids[i] % COL_COUNT
        data[brindex * gr: (brindex+1) * gr, bcindex * gc: (bcindex+1) * gc] = g
    return data
#Initial W,P
def iterateS(g):
    r, c = g.shape
    x = np.arange(0, c, dtype=int)
    for i in range(r):
        gi = g[i]
        aclist = np.full(200, "white")
        aclist[np.where(gi==1)] = "red"
        aclist[np.where(gi==2)] = "gold"
        aclist[np.where(gi==3)] = "tan"
```

```
Wy = np.where(gi==2)[0]
if g[i][0] == 0 :
    g[i][0]= 4
    P[i][0]= 1
aclist[np.where(gi==4)] = "aqua"
if len(Wy)!=0:
    for j in range(len(Wy)):
        Wyc = []
        gu = g[i-1][Wy[j]]
        gd = g[i+1][Wy[j]]
        gl = g[i][Wy[j]-1]
        gr = g[i][Wy[j]+1]
        if gr == 2 :
            Wyc.append(0.2)
        elif gr == 0 :
            Wyc.append(random.uniform(0, 99)/100)
        else:
            Wyc.append(0)
        if gu == 2 :
            Wyc.append(0.2)
        elif gu == 0 :
```

```
            Wyc.append(random.uniform(0, 99)/100)
        else:
            Wyc.append(0)
        if gl == 2 :
            Wyc.append(0.2)
        elif gl == 0 :
            Wyc.append(random.uniform(0, 99)/100)
        else:
            Wyc.append(0)
        if gd == 2 :
            Wyc.append(0.2)
        elif gd == 0 :
            Wyc.append(random.uniform(0, 99)/100)
        else:
            Wyc.append(0)
        W[i][Wy[j]] = Wyc
    y = np.full(200, 200 - i)
    plt.scatter(x, y, c=aclist)
    return g
#update W,P
def iterateT(g):
```

```
baseS = 0.44
for i in range(0,200):
    for j in range(0,200):
        x= j
        y= i
        u = y-1
        d = y+1
        l = x-1
        r = x+1
        if x+1 == m:
            r = x
        if x-1 == -1:
            l = x
        if y+1 == n:
            d = y
        if y-1 == -1:
            u = y
        dP = P[u][x]*W[u][x][2] + P[y][r]*W[y][r][3] + P[d][x]*W[d][x][0] +
P[y][l]*W[y][l][1] - P[y][x]*W[y][x][2] - P[y][x]*W[y][x][3] - P[y][x]*W[y][x][0] -
P[y][x]*W[y][x][1]
        if G[y][x] !=1 and G[y][x] !=3:
```

```
            if G[y][x] == 4:
                P[y][x] =1
            if G[y][x] != 2 :
                W[y][x] =  [random.uniform(0, 99)/100,random.uniform(0,
99)/100,random.uniform(0, 99)/100,random.uniform(0, 99)/100]
            else:
                if P[y][x]<=0.2:
                 W[y][x] = [0.2,0.2,0.2,0.2]
                else:
                 W[y][x] = [P[y][x],P[y][x],P[y][x],P[y][x]]
            if  P[y][x] >= 1:
                P[y][x] = 1
                G[y][x] = 4
            P[y][x] = round(P[y][x] + dP*baseS,2)
def showS(g,msg):
    r, c = g.shape
    x = np.arange(0, c, dtype=int)
    for i in range(r):
        gi = g[i]
        aclist = np.full(200, "white")
        aclist[np.where(gi==0)] = "white"
```

```
            aclist[np.where(gi==1)] = "red"
            aclist[np.where(gi==2)] = "gold"
            aclist[np.where(gi==3)] = "tan"
            aclist[np.where(gi==4)] = "aqua"
            y = np.full(n, m - i)
            plt.scatter(x, y,c=aclist,s=30,marker=".",alpha=(1))
        plt.title(msg)
        plt.rcParams["figure.figsize"] = (10,10)
        plt.show()
start=time.time()
x_avg = []
G = create_big()
G = iterateS(G)
for i  in range(5001):
    iterateT(G)
    if i in [0,1,100,500,1000,1250,1350,1500,2000,2500,3000,3500,4000,4500,5000]:
     msg = "T="+str(i)
     showS(G,msg)
     # calculate x average
     num = 0
     den = 0
```

```
    for x in range(1,m):
        x_summ = 0
        for y in range(n):
            x_summ += P[y][x]
        num += x_summ*(x**2)
        den += x_summ
    x_avg.append((num/den))
    print(x_avg)
   if len(np.where(G==0)[0])==0:
       showS(G,msg+"      im full")
       sys.exit()
fig=plt.figure()
ax=fig.add_axes([0,0,1,1])
ax.scatter([0,1,100,500,1000,1250,1350,1500,2000,2500,3000,3500,4000,4500,5000],
x_avg, color='#000000', s = 10)
ax.set_xlabel('T axis')
ax.set_ylabel('X squared avg axis')
ax.set_title('plot of <x^2> vs t')
plt.show()
end=time.time()
print ('running time:' +str((end-start)/60)+'min')
```